LAMB WAVE NONDESTRUCTIVE EVALUATION AND IMAGING ON PLATE-LIKE STRUCTURES

by

Zhaoyun Ma

Bachelor of Science
Wuhan University of Technology, 2012

Master of Science
University of Pittsburgh, 2016

Submitted in Partial Fulfillment of the Requirements

For the Degree of Doctor of Philosophy in

Mechanical Engineering

College of Engineering and Computing

University of South Carolina

2020

Accepted by:

Lingyu Yu, Major Professor

Victor Giurgiutiu, Committee Member

Yuh-Jin Chao, Committee Member

Paul Ziehl, Committee Member

Cheryl L. Addy, Vice Provost and Dean of the Graduate School

CHAPTER 5

FULLY NONCONTACT/REMOTE PL-SLDV LASER SYSTEM

The partial non-contact PZT-SLDV system adopted in Chapter 4 employs traditional contact type PZT as actuator and non-contact SLDV system as sensor. In NDE/SHM application, more than one actuator is often needed for large structure inspection. The attachment of these actuators are time and labor consuming and extra weight will be added on the host structure, which might modify the structure performance or increase the structure complexity. Non-contact type pulsed laser (PL) has caught researchers' attention since it can generate ultrasonic waves in both noncontact and remote manner [20, 33, 97]. This chapter focuses on the development and optimization of a fully non-contact NDE system, which employs PL and SLDV system for both noncontact and remote actuation and sensing. In addition, laser generated ultrasonic wave are analytically studied to better understand the laser working mechanism and thus improve the noncontact system performance.

5.1 PL-SLDV LAMB WAVE NDE SYSTEM CONFIGURATION

The PL-SLDV Lamb wave excitation and sensing capability is first confirmed. To achieve high signal quality, the PL excitation energy vs. signal-to-noise ratio (SNR) relationship is studied. Meanwhile, the averaging effect for sensing quality is also calibrated. With the acceptable excitation, Lamb wave modes are characterized both in time-space and

frequency-wavenumber domains. In addition, different surface enhancement has been tested to protect the specimen surface.

5.1.1 Lamb wave testing setup

The schematic design of the PL-SLDV system is illustrated in Figure 5.1 showing that PL is used for noncontact actuation instead of PZT transducer compared to Figure 4.1. The fully non-contact PL-SLDV laboratory setup is illustrated in Figure 5.2. A Quantel CFR400 Q-switch pulsed laser is adopted as the Lamb wave actuator. The excitation energy can be adjusted with a built-in attenuator from 0% ~ 100% of the full excitation energy (332 mJ). The wavelength of the pulsed laser is 1064 nm, which is in the invisible range. The pulse width is 7 ns and the near field beam diameter is 5.5 mm. The repetition rate of the pulsed laser is 20 Hz. Polytec PSV-400 SLDV is used as the multidimensional wavefield sensor. In order to improve the SLDV signal quality, reflective tapes are attached on the inspection area on the specimen surface. The PL and SLDV heads are placed on the opposite side of the testing plate and both laser heads are set normal to the specimen in this study. Q-switch box is used to send pulse trains to PL control box at a certain frequency to enable the PL actuation and trigger the SLDV measurement simultaneously. The enclosure is designed to fully cover the laser beam for safe laser operation.

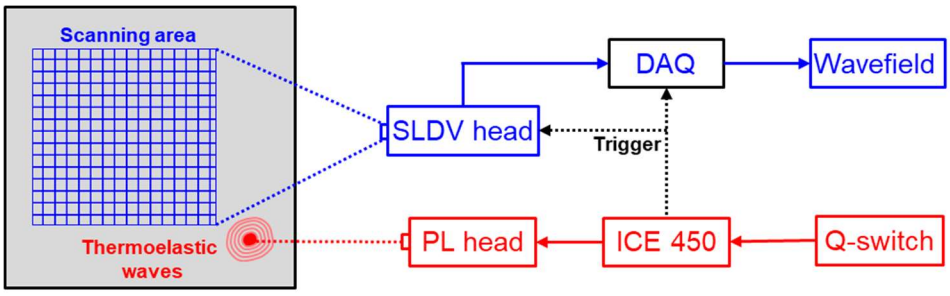

Figure 5.1 Non-contact PL-SLDV inspection system schematic design[47]

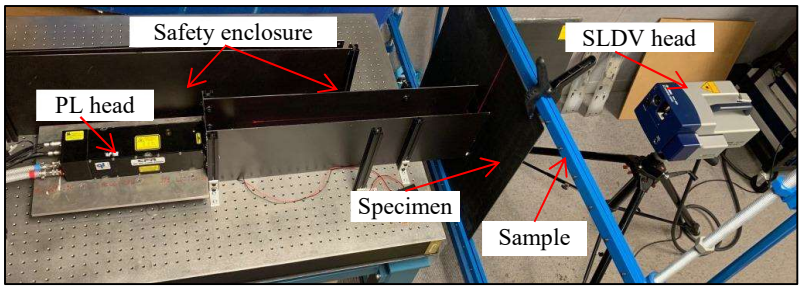

Figure 5.2 Non-contact PL-SLDV inspection system [100]

A 1-mm thick aluminum 2024-T3 plate (size: 610 mm × 610 mm × 1mm) is tested with clay added on the edge to minimize boundary reflections. Reflective tape is attached to improve the light reflection of the specimen surface to achieve high SNR. In this preliminary test, the initial excitation energy is set as 33 mJ (10% of the full energy). The sampling rate of SLDV is set 10.24 MHz and velocity decoder VD-09 is adopted which can measure up to frequency 1 MHz. The sensing point is set 60 mm away from the excitation. The measured waveform as well as its frequency spectrum are presented in Figure 5.3, which proves that Lamb waves have been successfully excited and recorded based on the proposed experimental setup.

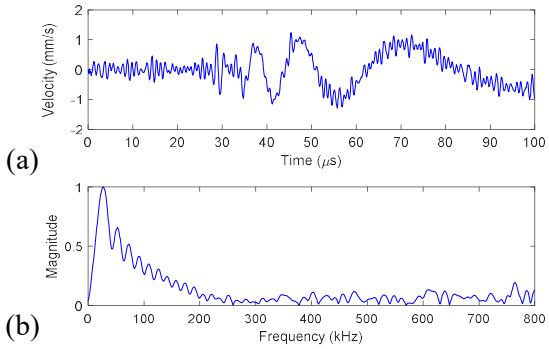

Figure 5.3 Waveform analysis: (a) waveform measured at 60 mm with excitation energy 33 mJ; (b) normalized frequency spectrum

5.1.2 PL Lamb wave excitation energy calibration

The Lamb wave excited in plate is known to be correlated with the input laser energy. Therefore, we first experimentally investigated the excitation energy for PL Lamb wave actuation. The waveforms at 60 mm away from the excitation point are recorded with different excitation energy set at 3% to 100% of the full power (330 mJ per pulse). Selected waveforms and corresponding frequency spectrum (10%, 50% and 100%) are plotted in Figure 5.4. Under low excitation energy, e.g. 33 mJ, the waveforms are noisy and Lamb wave modes are difficult to observe. At high excitation energy, e.g. 166 mJ, Lamb wave modes become recognizable where a faster wave package with lower strength (black circle) and a slower one with higher strength (red circle) are observed. The waveform quality improves with the increase of the energy, while the bandwidth of each waveform does not change significantly as shown in Figure 5.4.

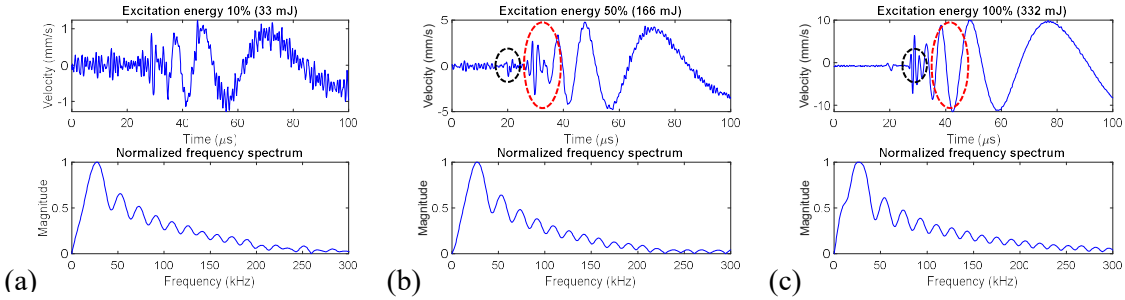

Figure 5.4 Waveforms at 60 mm and corresponding frequency spectrum at selected excitation energy: (a) 10%, (b) 50%, and (d) 100%, showing the SNR improves with excitation energy increase, while bandwidth does not change significantly

The signal quality and full width at half maximum (FWHM) bandwidth of the measured signals at different energy levels are evaluated. Two parameters are considered for the signal quality evaluated including SNR and root mean square deviation (RMSD). The SNR is calculated as:

$$SNR = \frac{P_{\text{signal}}}{P_{\text{noise}}} \tag{5.1}$$

where P_{signal} is the power of the whole signal, P_{noise} is the power of the floor noise. The RMSD is used for the signal noise evaluation, which is calculated as:

$$RMSD = \sqrt{\frac{\sum_i \left(v_i - v_{mean}\right)^2}{N}} \tag{5.2}$$

where v is the velocity and the v_{mean} is the mean value of the total signal. Note that the first 10 μs of the signal before any Lamb wave propagate to the selected distance 60 mm is used for calculation. The calculated signal evaluation results are presented in Table 5.1. The bandwidth is about 70 kHz for all signals, which does not change significantly when the energy increases. The SNR increases with the increase of energy, and the SNR is 10.27 dB at excitation energy:100 mJ, which is acceptable for future Lamb wave mode evaluation and damage detection. The RMSD stays around 0.2 mm/s when the energy level is below 50%, while it stays around 0.1 mm/s when the energy level is above 50%.

Table 5.1 PL Lamb wave signal evaluation results

EL (%)	**Energy (mJ)**	f_L **(kHz)**	f_H **(kHz)**	**BW (kHz)**	**SNR (dB)**	**RMSD of Noise (mm/s)**
3%	10	11.25	90.63	79.38	0.59	0.20
10%	33	11.25	76.88	65.63	4.77	0.17
20%	66	11.88	77.50	65.63	8.11	0.21
30%	100	11.25	78.13	66.88	10.27	0.26
40%	133	11.88	77.50	65.63	12.94	0.27
50%	166	11.88	75.63	63.75	14.19	0.24
60%	199	11.88	76.88	65.00	17.55	0.10
70%	232	11.25	76.25	65.00	18.37	0.12
80%	266	9.38	77.50	68.13	19.86	0.11
90%	299	10.00	76.88	66.88	22.04	0.09
100%	332	7.50	76.25	68.75	22.70	0.09

5.1.3 PL Lamb wave sensing average calibration

To acquire signals with good quality for effective inspection, the sensing average is calibrated by waveform analysis. The same experimental setup and specimen are used with excitation energy 33 mJ (10% of full energy). The waveform is recorded at 80 mm away from the excitation point, which is the furthest point in potential scanning set. Averaging with 1-8 times are conducted for the waveform measurement. Selected waveforms with averaging 1, 4 and 8 times are shown in Figure 5.5. The signal evaluation including SNR and RMSD value is shown in Table 5.2. As shown in the waveforms, the signal quality improves with the averaging times, which is indicated by the SNR increase and RMSD decrease. With averaging 4 times, the SNR reaches 10.29 dB, which is acceptable for signal quality. More averaging times can be adjusted according to the inspection requirement in the future research.

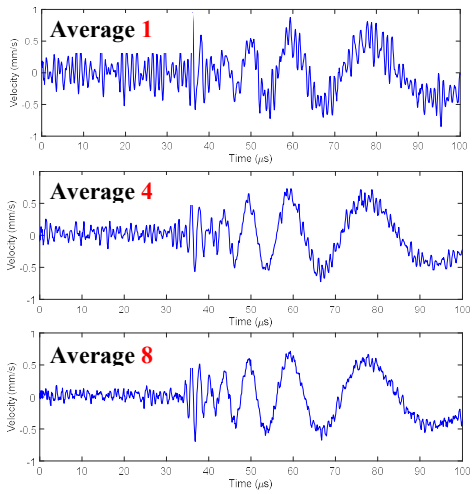

Figure 5.5 Waveforms recorded at 80 mm with different averaging times

Table 5.2 Signal evaluation with different averaging

Average	1	2	3	4	5	6	7	8
SNR (dB)	5.47	6.95	9.34	10.29	10.39	10.76	12.06	13.56
RMSD of noise (mm/s)	0.1699	0.1410	0.1045	0.0941	0.0938	0.0895	0.0754	0.0641

In summary, the relationships of bandwidth change with respect to (w.r.t.) excitation energy, SNR change w.r.t. excitation energy, and SNR change w.r.t. average times are presented in Figure 5.6. Conclusions can be drawn that the excitation energy change does not affect the signal bandwidth significantly, while the increase of excitation energy can improve the signal SNR. In addition, the signal SNR will improve if more averages are used for measurement.

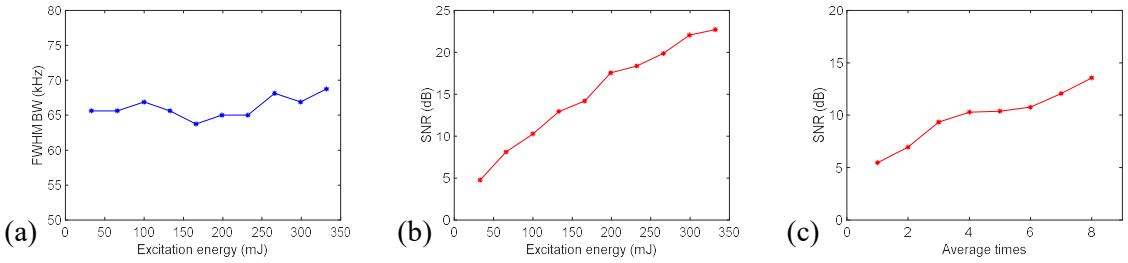

Figure 5.6 Signal evaluation through: (a) bandwidth change with w.r.t. excitation energy, (b) SNR change w.r.t. excitation energy, and (c) SNR change w.r.t. average times

5.1.4 PL Lamb wave modes characterization

With the calibrated parameters for the PL-SLDV system, Lamb wave modes are further characterized for future inspection with SLDV line scans. The scanning lines are from 20 mm to 80 mm away from the PL excitation. Different excitation energy: 10, 20, 40, 70 and 100 mJ, are selected for Lamb wave actuation in order fully understand the system performance. Based on last subsection, 5 averages are used for the SLDV sensing to obtain effective inspection signals. The selected time-space wavefields with excitation energy 20, 40, and 100 mJ are plotted in Figure 5.7. With low excitation energy, faster S_0 mode is weak and difficult to observe while slower A_0 mode is strong and readily observed. With higher excitation energy 40 and 100 mJ, the S_0 mode becomes stronger and more visible,

followed by a stronger still A_0 mode. With increase of the excitation energy, the Lamb wave mode becomes stronger and clearer to distinguish.

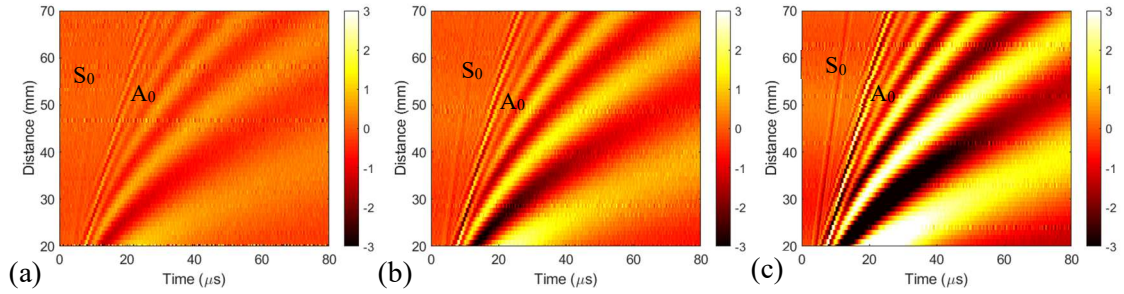

Figure 5.7 Time-space wavefields, measured with excitation energy: (a) 20, (b) 40, and (c) 100 mJ

The frequency-wavenumber (f-k) analysis is also performed to further confirm the excited wave modes. The f-k results as well as the theoretical dispersion curves are presented in Figure 5.8, where consistent wave modes are observed compared to time-space wavefield results. With lower excitation energy, only A_0 mode can be observed and it matches the theoretical A_0 well. With higher excitation energy, both weaker S_0 and stronger A_0 can be observed and they agree well with the theoretical dispersion curves.

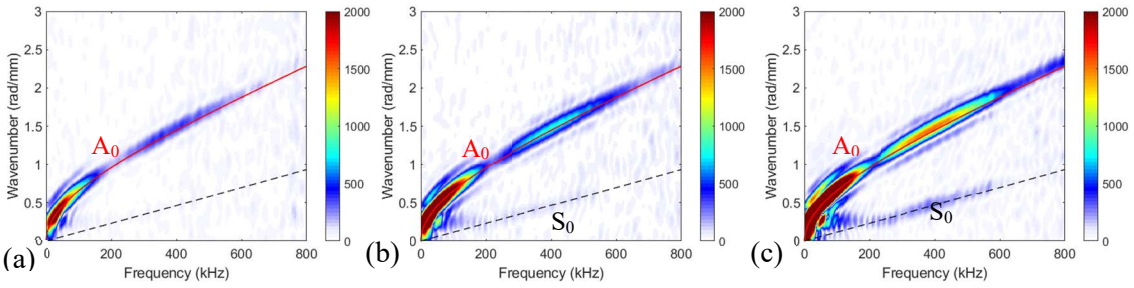

Figure 5.8 Frequency-wavenumber spectra with excitation energy: (a) 20, (b) 40, and (c) 100 mJ

5.1.5 PL Lamb wave excitation surface enhancement

During the preliminary tests, surface burn damage is observed at high energy excitation such as 40, 70 and 100 mJ. The surface burn is showing as whitish dust shown in Figure

5.9a. To avoid the surface damage caused by burning, two types of surface protection are tested on the same aluminum plate. The two surface protections are aluminum foil (surface condition-1, SC-1) and copper foil (surface condition-2, SC-2) with 0.7 mm thickness and around 8 mm diameter. The surface protections are bonded on the target excitation point with M-bond 200 adhesive to guarantee strong coupling between the protections and specimen. The raw surface condition (SC-0) is set as the reference for comparison and evaluation. Three line-scans are performed by SLDV under the three surface conditions: SC-0, SC-1 and SC-2 with 100 mJ PL excitation. The line scan setup is shown in Figure 5.9b. After the experiments, the surface condition is observed and recorded first as shown in Figure 5.9c. After the experiment (about 600 shoots by PL on the excitation point), whitish dust is observed for SC-0 and SC-1, while no significant change is observed for SC-2. After removal of the surface protections, no surface burn appears on the specimen for both SC-1 and SC-2, which means the specimen is protected well by both two protections.

To achieve equivalent Lamb wave actuation and signal quality as with raw surface condition (SC-0), waveform and wavefield analysis are performed to further evaluate the two surface protections. The waveforms at x = 60 mm and the corresponding frequency spectrum for the three surface conditions are shown in Figure 5.10. From the waveform analysis results, the signal strength for SC-1 is still good compared to SC-0, and the SNR for SC-1 is the highest which indicates that the SNR improves after attaching the aluminum surface protection. The RMSD for SC-1 is lower than that for SC-0, thus, the signal for SC-2 is less noisy than SC-1. For SC-2 (copper surface protection), the signal strength and SNR are much lower than SC-0. The frequency spectrum does not change significantly for

the three conditions. In conclusion from the waveform analysis, the aluminum foil is qualified for surface protection of PL excitation for aluminum plates, while the copper is not a good candidate.

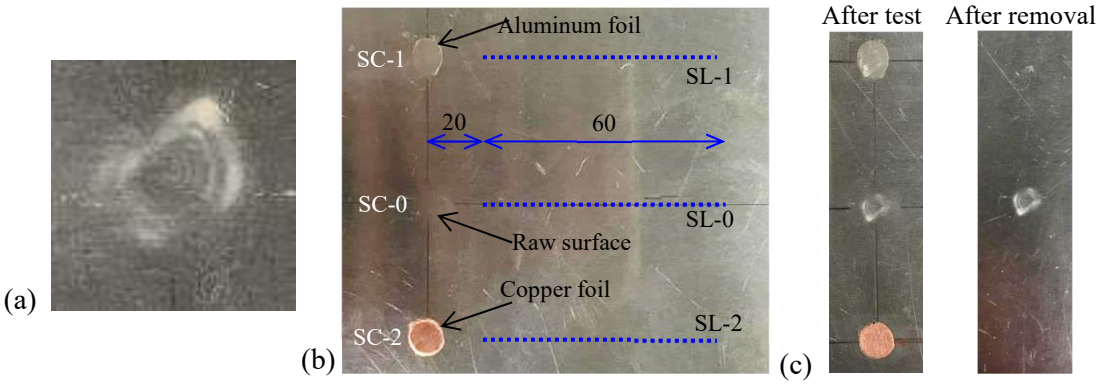

Figure 5.9 Surface enhancement setup: (a) example burn with 100 mJ excitation (zoom in), (b) Line scan setup for surface protections, and (c) Surface conditions after the experiments, and after protection removal

In addition, the Lamb wave characterization is also performed for the three surface conditions to guarantee PL Lamb wave successfully excited in the testing specimen. As shown in the wavefield $v(t,x)$ in Figure 5.11, weaker and faster S_0 mode and stronger and slower A_0 mode are both excited in SC-0 and SC-1, while only A_0 is excited for SC-2. In the *f-k* spectrum, the same phenomenon is observed. Note that the red and black line are the theoretical A_0 and S_0 dispersion curves in a 1-mm aluminum 2024-T3 plate. Stronger A_0 and weaker S_0 are observed in SC-0 and SC-1, while only A_0 is observed for SC-2. From the wavefield and *f-k* spectrum results, SC-1 with aluminum surface protection shows that the comparable Lamb wave modes are excited as SC-0 with raw surface condition, while only weak A_0 is excited in SC-2. Combing the conclusion obtained from surface condition visual inspection, waveform and wavefield analysis results, the SC-2 with aluminum surface protection is the best candidate for future PL Lamb wave excitation on aluminum plates.

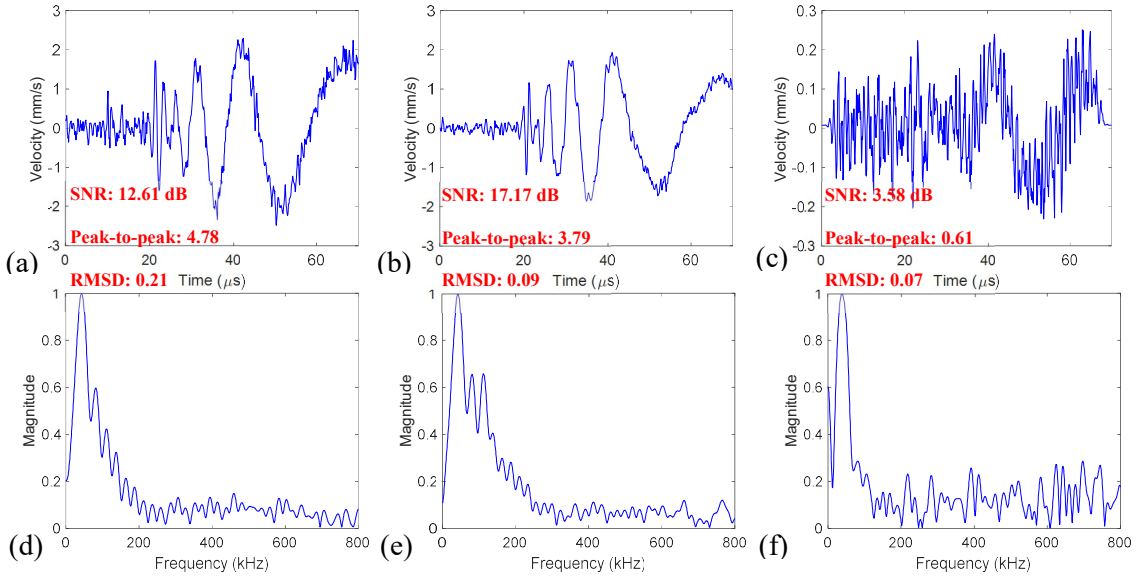

Figure 5.10 Waveforms at 60 mm away from the PL excitation: (a) SC-0, (b) SC-1, and (c) SC-2; the relative frequency spectra: (d) SC-0, (e) SC-1, and (f) SC-2

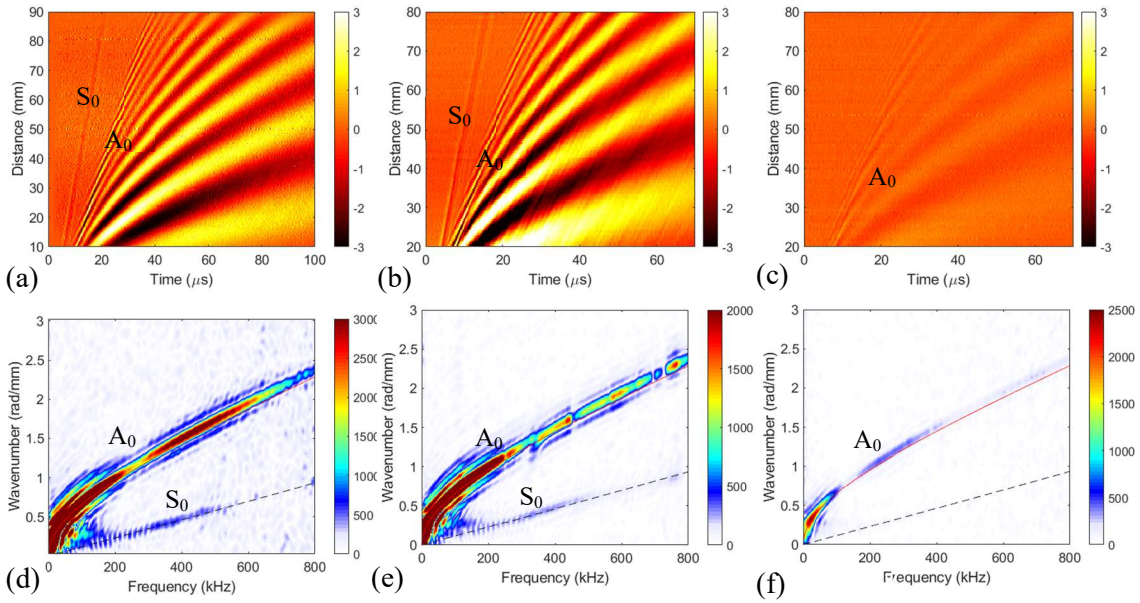

Figure 5.11 Wavefield and *f-k* spectrum results of three surface conditions: wavefield of (a) SC-0, (b) SC-1, and (c) SC-2; the relative frequency spectra of: (d) SC-0, (e) SC-1, and (f) SC-2

5.2 DAMAGE INSPECTION ON AN ALUMINUM PLATE

With the demonstrated capability of PL Lamb wave actuation and optimal setup, this chapter focuses on application of the non-contact PL-SLDV system to inspect metallic

plates with simulated damage (surfaced-bonded quartz rod and machine milled crack). Both 1D and 2D inspection are performed and wavefield analysis is conducted. Lamb wave based imaging is also performed for further damage evaluation through three imaging methods: wavefield imaging, filtering reconstruction imaging and wavenumber imaging.

5.2.1 Experimental setup

Three 1-mm aluminum 2024-T3 plates are tested in the following experiments: one pristine plate, one damaged plate with surface bonded quartz rod shown in Figure 5.12a (10-mm thickness and 10-mm diameter), and one damaged plate with computer numerical control (CNC) machine milled crack shown in Figure 5.12b (0.5-mm width and 10-mm length). The specimen schematic is shown in Figure 5.12c for 1D line inspection and Figure 5.12d for 2D area inspection with spatial resolution of 1 mm. Cartesian coordinates are used with excitation point set as origin and damage located at y=70 mm. The PL excitation energy is set as 100 mJ, and surface protection (0.7-mm thick aluminum foil) is attached at the origin. 10 averages are used in order to get a higher SNR for better inspection results.

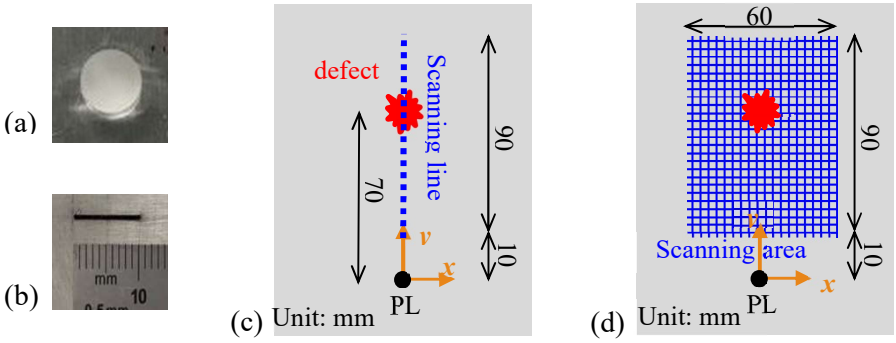

Figure 5.12 Schematic of specimen set up: (a) surface bonded quartz rod, (b) machine milled crack, (c) 1D line inspection set up, and (d) 2D area inspection setup

5.2.2 1D inspection results

The acquired time-space wavefields along the scanning line are plotted in Figure 5.13a, b and c. Through 2D Fourier transform of the wavefield data, *f-k* spectra are obtained as shown in Figure 5.13d, e and f. For pristine plate, S_0 and A_0 Lamb wave modes are observed. The relative *f-k* spectrum (Figure 5.13d) is consistent with the wavefield result. The wavefield for quartz plate also shows that two incident wave modes S_0 and A_0. However, reflected waves appear at x=65 mm where the quartz edge is, and weak transmitted waves are observed after waves interacted with the quartz. In the corresponding *f-k* spectrum (Figure 5.13e), negative A_0 is observed. The wavefield for crack plate also shows similar wave phenomenon as quartz plate. The difference is that the reflected waves are clearer, and the transmitted waves are stronger. In the corresponding *f-k* spectrum in Figure 5.13f, negative A_0 is also observed as expected.

With 1D Lamb wave inspection, the quartz and crack are both detected and localized using wavefield analysis. However, the location of damage is not indicated in the *f-k* representations. Thus, short space-wavenumber (*x-k*) analysis is performed to further localize the damage and capture the wavenumber variation along the scanning line. 90 kHz is selected as the interested frequency since A_0 is stronger at lower frequency. The calculated *x-k* spectrum at 90 kHz for the three plates are plotted in Figure 5.13g, h and i respectively. In the *x-k* spectrum of pristine plate (Figure 5.13g), only positive A_0 is observed. Compared to pristine plate, negative A_0 appears before x=70 mm for quartz plate (Figure 5.13h). This indicates that incident waves propagate and reflect after interacting with the quartz. After 70 mm, only weak positive A_0 is observed, which is consistent with the relative wavefield where transmitted waves are relatively weak. In addition, new

wavenumbers lower than A_0 wavenumber (0.62 rad/mm) are observed. For crack plate, strong negative A_0 is observed at the crack location (x=70 mm), while considerable waves transmitted after the crack as shown in Figure 5.13i. Moreover, new wavenumbers higher than A_0 wavenumber are observed.

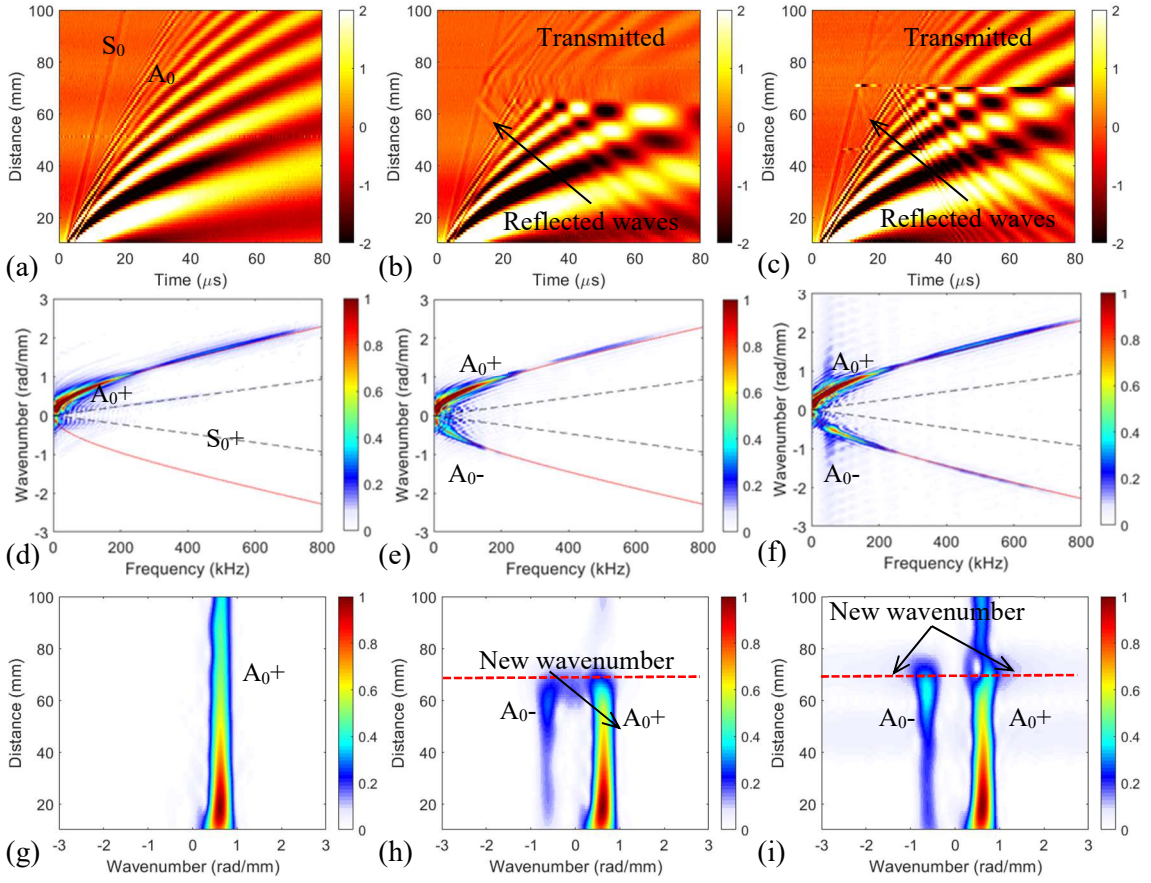

Figure 5.13 Time-space wavefields of: (a) pristine plate, (b) quartz plate, and (c) crack plate, showing Lamb wave interaction with different damage in each plate; frequency-wavenumber spectra of: (d) pristine plate, (e) quartz plate, and (f) crack plate, showing Lamb wave modes in frequency-wavenumber domain; short space-wavenumber spectra at 90 kHz of: (g) pristine plate, (h) quartz plate, and (i) crack plate, showing different wavenumber variation along the scanning line for each plate

5.2.3 2D inspection results

In this section, 2D inspection and wavefield analysis are performed. The space wavefield at 17, 26 and 40 μs are captured and plotted in Figure 5.14 for each plate to show Lamb

wave interaction with the selected damage. In Figure 5.14a, d and g, the 2D Lamb wave propagation in the pristine plate is illustrated, where the wave front is circular, and waves propagate smoothly along time. The 2D Lamb wave propagation in the quartz plate is shown in Figure 5.14b, e and h. At 17 μs, mode conversion from S_0 to A_0 is observed at y=70 mm (Figure 5.14b), and waves scattered since the quartz works as a new scatter source. After waves bypass the quartz, they split from around y=65 mm as shown in the wavefield at 40 μs (Figure 5.14h), resulting in that very little waves transmitted. For crack plate, weak reflective waves from S0 are observed at 17 μs (Figure 5.14c), while strong reflected waves from A_0 are observed at 26 μs at y=70 mm. After that, waves bypass the crack and transmitted waves are observed in the wavefield at 40 μs (Figure 5.14i). With the acquired time-space wavefields, the damage are localized at around 70 mm for both quartz and crack plates.

In order to observe the 2D inspection results in another perspective, the *f-k* analysis is performed through 3D Fourier transform. The obtained wavenumber spectrum at 90 kHz for pristine, quartz and crack plate are plotted in Figure 5.15a, b and c respectively. Since A_0 is dominate at this interested frequency, only wavenumber changes related to A_0 are discussed. In the wavenumber spectrum for pristine plate (Figure 5.15a), strong incident A_0 is observed, which matches well with the theoretical A_0 wavenumber curve (0.62 rad/mm). Compared to pristine condition, reflected A_0 appears in the wavenumber spectrum for quartz and crack plate. In addition, new wavenumber components are observed: lower wavenumber components (<0.62 rad/mm) for quartz plate while high wavenumber components (> 0.62 rad/mm) for crack plate.

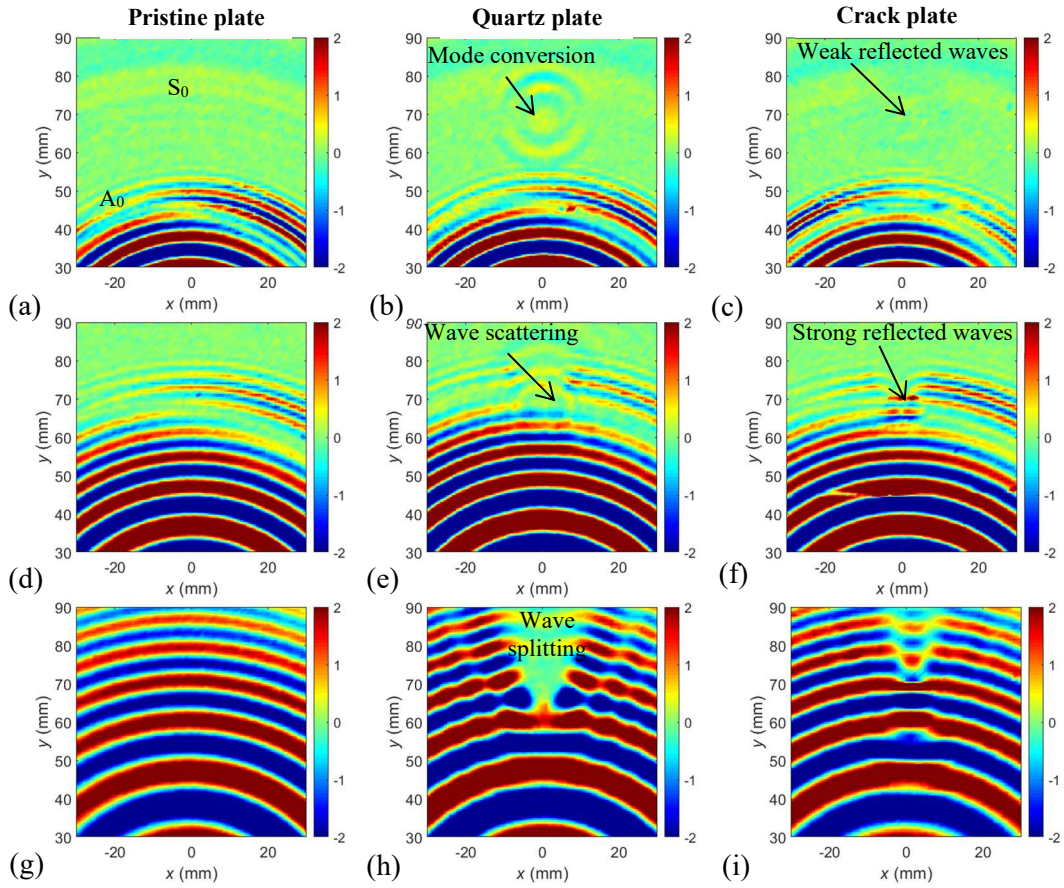

Figure 5.14 Wavefield snapshots at different times, wavefields at 17 μs for: (a) pristine plate, (b) quartz plate, and (c) crack plate; wavefields at 26 μs for: (d) pristine plate, (e) quartz plate, and (f) crack plate; wavefields at 40 μs for: (g) pristine plate, (h) quartz plate, and (i) crack plate, showing Lamb wave interaction with different damage differently

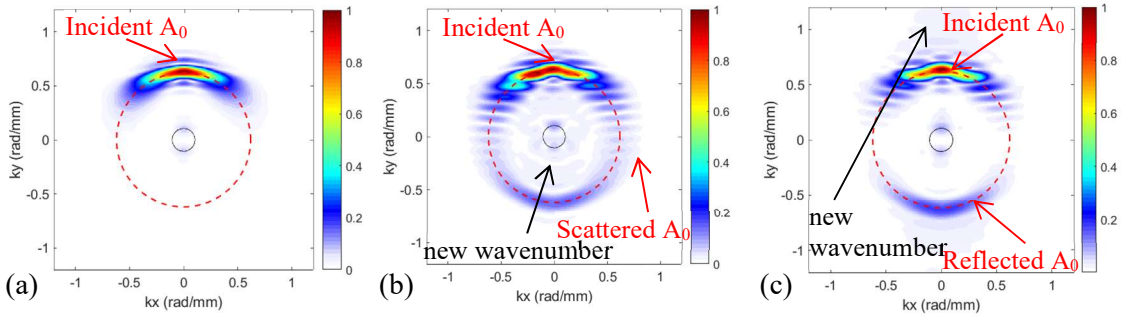

Figure 5.15 Wavenumber spectrum at 90 kHz for (a) pristine plate, (b) quartz plate, and (c) crack plate. Note: the red dash line is the theoretical A_0 wavenumber curve at 90 kHz, and the black line is the theoretical S_0 wavenumber curve at 90 kHz.

In order to further evaluate the damage, Lamb wave imaging process is applied to the 2D wavefield data using different imaging methods presented in Chapter 4.3, including wavefield imaging, filtering reconstruction imaging and wavenumber imaging methods.

➢ *Wavefield imaging results*

Wavefield imaging is the most direct way to diagnose the testing specimen. The wavefield images are generated by calculating the maximum absolute amplitude for each scanning point, and the results are presented in Figure 5.16. For pristine plate, the energy is the largest in the energy source (excitation at origin), and it drops gradually along the propagation distance. Obvious energy drop is observed in the wavefield imaging of quartz plate when the waves interact with the quartz edge where x=65 mm. After pass the quartz, the wave energy split by the quartz. This phenomenon is consistent with the wave phenomenon observed in the time-space wavefield shown in Figure 5.14h. For crack plate, energy increases at crack location, and standing waves formed before the crack due to the interference between the incident and reflected waves.

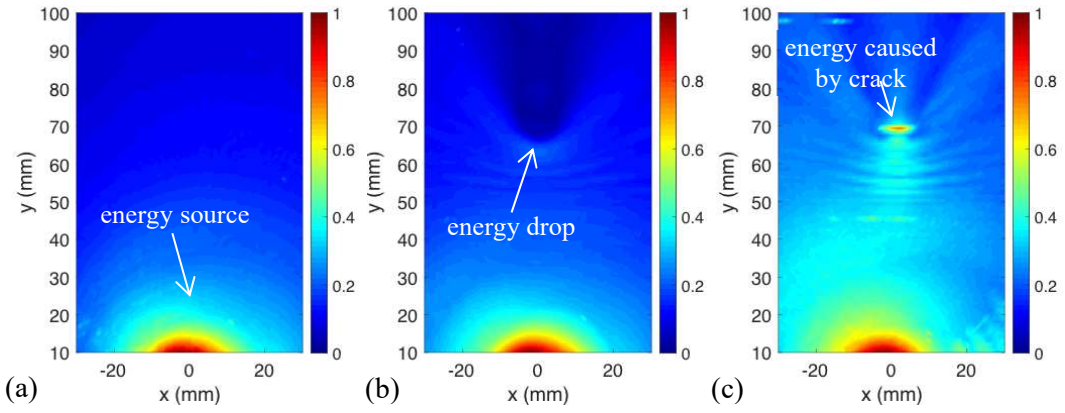

Figure 5.16 Wavefield imaging results for: (a) pristine plate, (b) quartz plate, and (c) crack plate

➢ *Filtering reconstruction imaging results*

In the *f-k* analysis, new wavenumber components are observed: low wavenumber components for quartz plate and high wavenumber components for damage plate compared to A_0 wavenumber. In this part, the filtering technique will be used to extract the new wavenumber components caused by damage, and then the extracted information will be inversed to reconstruct an energy image.

Since new wavenumber components in the *f-k* spectrum for quartz plate are lower than the A_0 wavenumber and higher than S_0 wavenumber as shown in Figure 5.17a, a band pass filter as shown in Figure 5.17b is used to extract the new wavenumber components (Figure 5.17c) between S_0 (0.1 rad/mm) and A_0 (0.62 rad/mm). The filtering reconstruction imaging is generated by calculating the energy map of the inversed filtered *f-k* spectrum. The same filtering process is repeated for pristine plate for comparison purpose. The normalized filtering reconstruction images for pristine and quartz plate are shown in Figure 5.18. In the generated image for pristine plate, the energy induced by damage is almost zero in the scanning area. For quartz plate, a high energy area appears near the quartz edge at about x=65 mm, while no obvious energy change for the pristine plate.

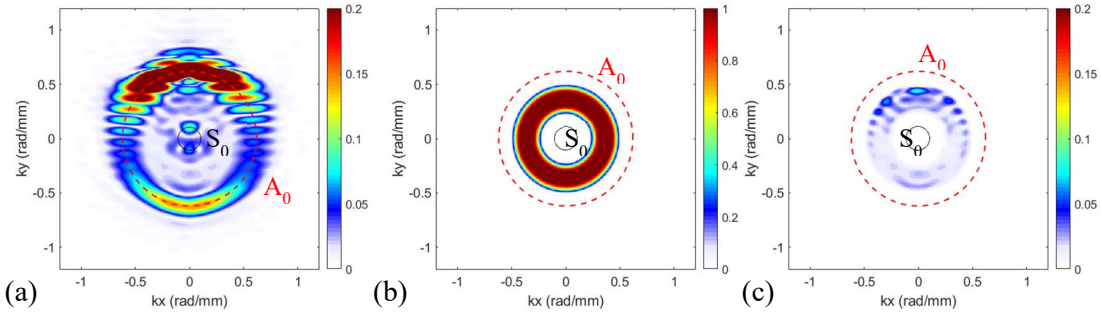

Figure 5.17 Filtering process using band pass filter for quartz plate: (a) original *f-k* spectrum, (b) band pass filter, and (c) filtered *f-k* spectrum

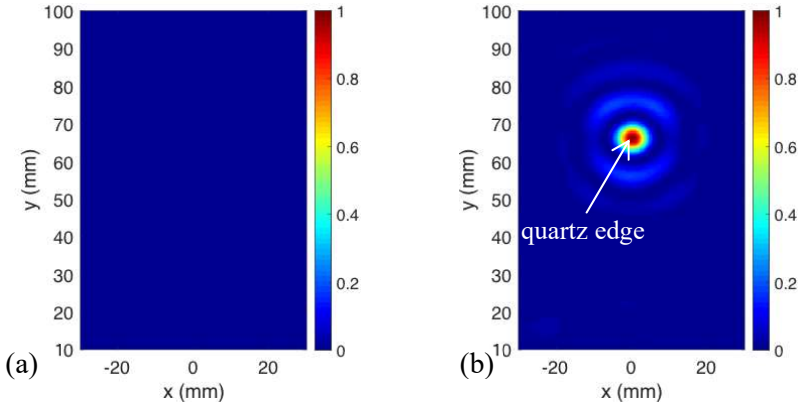

Figure 5.18 Filtering reconstruction images for:(a) pristine plate, and (b) quartz plate

Compared to the pristine plate, new wavenumber components in the *f-k* spectrum for crack plate are higher than the A_0 wavenumber as shown in Figure 5.19a. Thus, a high pass filter (Figure 5.19b) is used to extract the new wavenumber components. The normalized filtering reconstruction images for pristine and crack plate are plotted in Figure 5.20. In the image for pristine plate, the energy induced by damage is almost zero in the scanning area. For crack plate, a high energy area appears at the crack location, where x=70 mm. With the filtering reconstruction imaging method, the crack location is highlighted compared to the pristine plate.

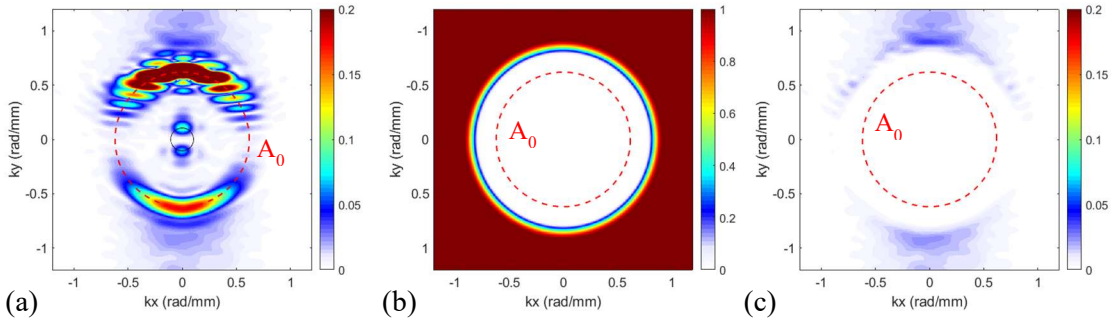

Figure 5.19 Filtering process using high pass filter for crack plate: (a) original *f-k* spectrum, (b) high pass filter, and (c) filtered *f-k* spectrum

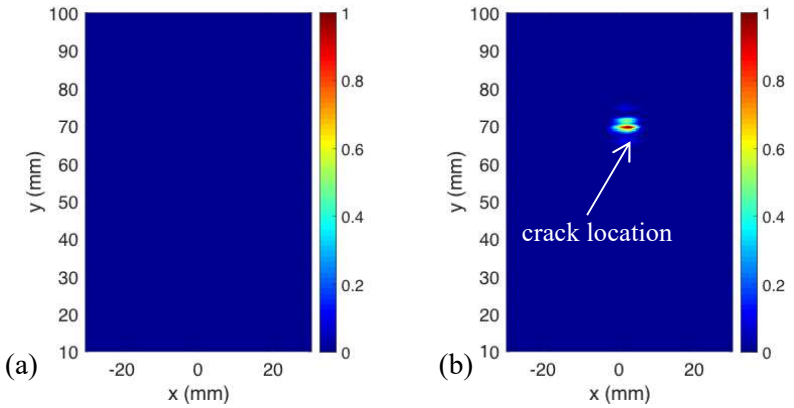

Figure 5.20 Filtering reconstruction images for:(a) pristine plate, and (b) crack plate

➢ *Wavenumber imaging results*

With the frequency-wavenumber analysis, the wavenumber information $\mathbf{k}(f)$ at interested frequency 90 kHz is obtained. However, the corresponding space information $\mathbf{x}$ relates to the wavenumber is lost during the Fourier transform. With short space Fourier transform, the space information related to each location can be retained in the wavenumber spectrum, resulting in a wavenumber distribution function in the scanning area as $\mathbf{k}(\mathbf{x}, f)$. The detailed derivation of the wavenumber imaging can be found in Chapter 4.3.

The wavenumber imaging for the three tested plates are generated and presented in Figure 5.21a. The overall wavenumber value is around 0.6 rad/mm for the pristine plate in the scanned area. Compared to pristine plate, low wavenumber around 0.2 rad/mm appear at the edge of quartz for the quartz plate as shown in Figure 5.21b. This low wavenumber phenomenon is consistent with low wavenumber observed in the wavenumber spectrum in Figure 5.17a. For the crack plate, high wavenumber values with red color appear at the crack location as shown in Figure 5.21c, which is consistent with the new high wavenumber components observed in the wavenumber spectrum in Figure 5.19a. With the

short space wavenumber algorithm, the quartz and crack locations are detected and visualized with distinguish different wavenumber values in the wavenumber image.

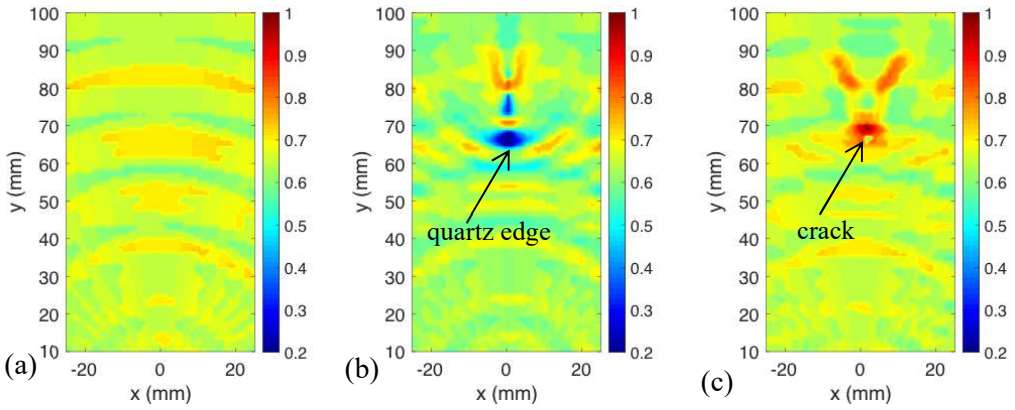

Figure 5.21 Wavenumber imaging results for:(a) pristine plate, (b)quartz plate, and (c) crack plate

5.3 DAMAGE INSPECTION ON AN COMPOSITE PLATE

With the presented PL-SLDV Lamb wave inspection system, a composite plate with simulated damage is inspected and evaluated compared to a pristine plate. The simulated damage is a 10 mm diameter circular quartz rod bonded on the specimen surface. The composite plate is a 8-ply quasi-isotropic plate with layup $[0/45/90/-45]_s$. The dimension of the plate is 610 × 610 × 2.54 (unit: mm). 1D inspection is performed first for a quick Lamb wave characterization as well as to capture the wave damage interaction characteristics. 2D inspection is then further conducted in order to capture more details and quantify the damage.

5.3.1 Experimental setup

The inspection actuation and sensing setup is illustrated in Figure 5.22 with Figure 5.22a for 1D inspection and Figure 5.22b for 2D inspection respectively. Cartesian coordinates are used in this study with the origin set at the excitation location. A 0.13 mm thick and 8

mm diameter aluminum foil is attached on the excitation point to protect the surface from burning. The quartz is located at y=70 mm. The scanning line is along y direction (90º fiber direction) from 10 mm to 100 mm for 1D inspection, while the scanning area is about 60 mm by 90 mm for 2D inspection. The SLDV spatial resolution is set as 1 mm for both 1D and 2D inspection. The pulsed laser excitation energy is set as 100 mJ for proof of concept study. Other remaining settings are the same as previous section.

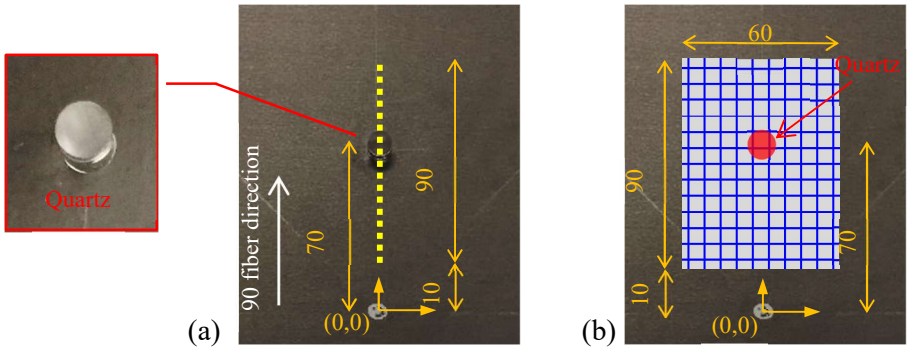

Figure 5.22 Actuation and sensing schematic: (a) 1D inspection, and (b) 2D inspection

5.3.2 1D inspection results

The acquired time-space wavefield of the pristine and damage plate is presented in Figure 5.23a and Figure 5.23b respectively. In the pristine plate wavefield, only two incident Lamb wave mode are observed: fast, weak, and nondispersive S_0 while slow, strong, and dispersive A_0. In the damage plate wavefield, S_0 to A_0 mode conversion appeared except the incident waves when waves interacted with the bonded quartz (approximately at y = 65 mm, where the quartz edge is). In addition, A_0 reflections are observed clearly at the quartz edge. In order to further capture the wave-damage interaction characteristics, 2D Fourier transform [62] is conducted to transfer the time-space wavefield data into frequency and wavenumber domain. The obtained frequency-wavenumber (f-k) spectra are plotted in Figure 5.23c and Figure 5.23d respectively, as well as theoretical dispersion curves for

comparison purpose. In the f-k spectrum of pristine plate, two positive wave modes are observed which matches theoretical S_0 and A_0 dispersion curves, which confirmed the wave modes characterization in the wavefield. The S_0 mode is weaker and the A_0 mode is significantly stronger, which agrees with the wave phenomena observed in the time-space wavefield. In addition, the A_0 components concentrated on mostly at the low frequency range (lower than 200 kHz). Different from pristine plate, reflected A_0 is observed in addition to the incident S_0 and A_0 modes, indicating that damage may exist in the structure.

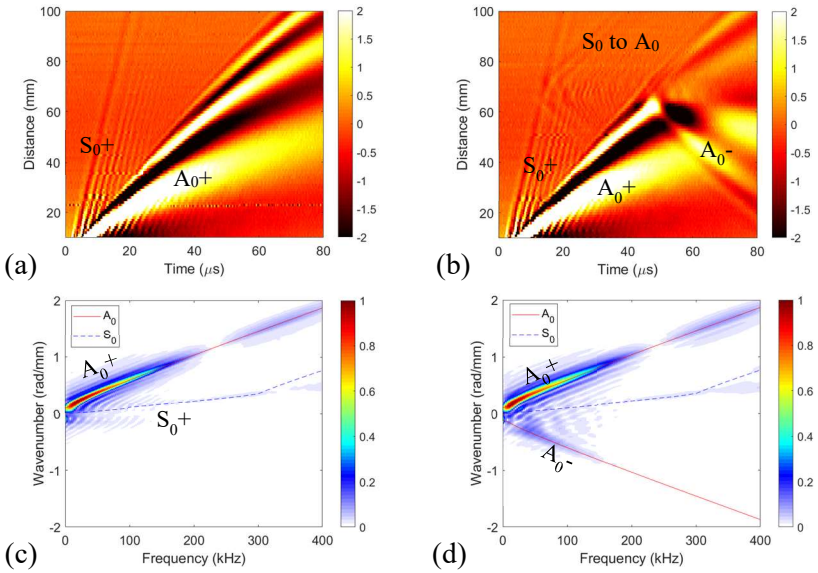

Figure 5.23 1D inspection results: time-space wavefield of (a) pristine plate, and (b) damage plate; frequency-wavenumber spectrum of (c) pristine plate, and (d) damage plate

5.3.3 2D inspection results

The SLDV acquired time-space wavefields at 60 μs of the pristine plate and damage plate is shown in Figure 5.24a and Figure 5.24d respectively to visualize the wave-damage interaction. Compared to the pristine plate, where only incident waves exist, scattered waves are observed when the waves interact with the quartz damage. In addition, the waves are blocked along *y* direction due to the existence of the quartz damage. The Lamb wave-damage interaction characteristics in the frequency-wavenumber domain is also explored

through 3D Fourier transform. The obtained wavenumber spectra at selected frequencies (90 and 150 kHz) are presented in Figure 5.24. In the wavenumber spectrum of pristine plate at both 90 kHz and 150 kHz, incident A_0 is observed and agrees with the theoretical wavenumber curve well (red dash line). In the wavenumber spectrum of damage plate, scattered A_0 is observed in addition to the incident A_0, and some new wavenumbers (lower than A_0 wavenumber) are observed for both frequencies. However, the scattered A_0 and new wavenumber components are more obvious and stronger at 90 kHz than that at 150 kHz. Thus, 90 kHz is more preferential for further imaging processing such as filtering based imaging or wavenumber imaging.

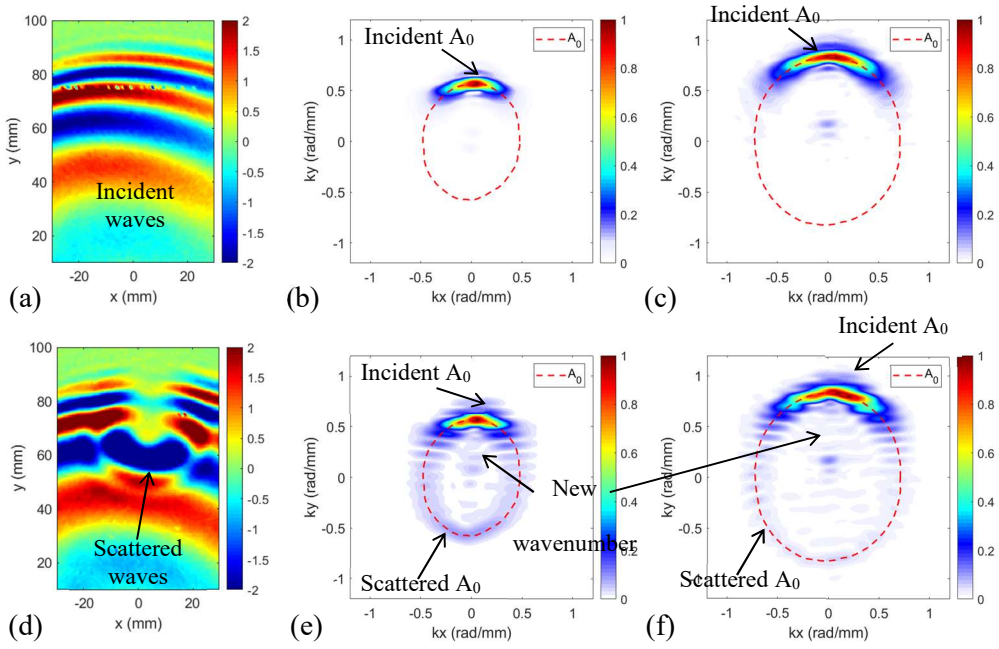

Figure 5.24 2D wavefiled analysis results: time-space wavefield of (a) pristine plate, and (e) damage plate; wavenumber spectrum at 90 kHz of (b) pristine plate, and (e) damage plate; and wavenumber spectrum at 150 kHz of (c) pristine plate, and (f) damage plate

In order to further evaluate the damage, Lamb wave imaging process is applied to the acquired 2D wavefield data. First, wavefield images are generated and presented in Figure 5.25a and Figure 5.25d for the pristine and damage plate respectively. The energy field

image of pristine plate shows that the wave energy attenuates with wave propagation. Note that the red line at about y=75 mm is not a damage and it is caused by overlapping of the attached reflective tape, which can be avoided by using wipe-off reflective sprays. For the damage plate, a sharp energy drop is observed at y=65 (the quartz edge location) and the wave energy keep decreasing after the quartz, indicating that most of the wave energy is scattered due to the quartz. The bottom part of the quartz profile is indicated as a circular shape which agrees well with the quartz dimension (the white dash circle). Secondly, filtering reconstruction imaging process is applied by using a low pass filter ($|k| < 0.38$ rad/mm) to filter out the new lower wavenumbers. The resulting images are presented in Figure 5.25b and Figure 5.25e for the pristine and damage plate respectively. The detailed data processing procedures can be found in previous section. One can see that the defect location is highlighted at round y = 65 mm, which is the quartz edge location. Lastly, space-wavenumber images are obtained for both the pristine and defect plate through windowing 3D Fourier transform. The space-wavenumber images are plotted in Figure 5.25c and Figure 5.25f respectively. One can see that the wavenumber value for pristine plate is around 0.55 rad/mm, while for the damage plate, much lower wavenumbers appeared at the quartz location, which is highlighted with green and blue color.

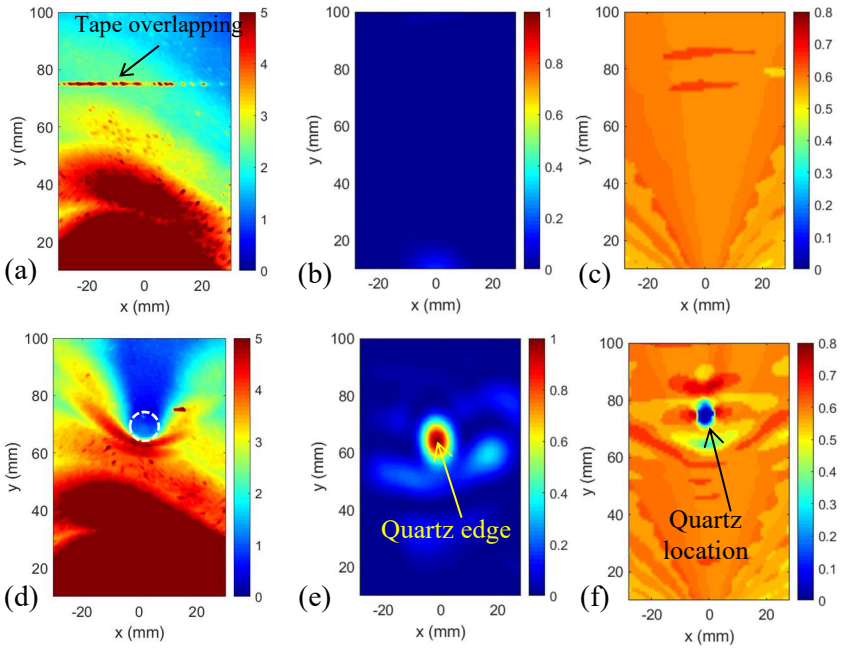

Figure 5.25 2D imaging results: energy field images of (a) pristine plate, and (d) damage plate; filtering reconstruction images of (b) pristine plate, and (e) damage plate; wavenumber images of (c) pristine plate, and (f) damage plate

CHAPTER 7

NDE/SHM APPLICATIONS ON COMPOSITE STRUCTURES

Composite materials are widely used in aerospace and aeronautical industries, and the interest of using more advanced composites is growing high [110] because of their advantages for light weight, high strength, and flexibility for engineering design. The large use of composites necessitates the development of appropriate nondestructive evaluation (NDE) methods to detect and quantify defects and damage in composites [111]. Various defects such as fiber waviness or undesirable material may appear in composite structures during the manufacturing process [112]. Wrinkles or waviness are common when adding new layers [113] or during curing with temperature gradients [111]. Wrinkles/waviness can be in-plane or out-of-plane: in-plane wrinkles occur in thin composite more often since the out-of-plane motion of the fibers is restricted, while out-of-plane wrinkles occur in thick composite plate more easily due to the possibility of large temperature gradients [114]. Wrinkles/waviness will cause significant degradation of the composite strength and can weaken the composite structure performance. Debonding occurs when an adhesive stops adhering to an adherend or if physical or mechanical forces that hold the bond together are broken while delamination is a failure in a laminate which leads to separation of the layers or plies. All these undesirable defects affect the mechanical properties and structural overall performance [112], and may further jeopardize the safety of space structures during operation. Thus nondestructive evaluation methods that are suitable for a wide range of defects are highly needed [110, 115] for ensuring safety and reliability of

aeronautic vehicles [116, 117]. In this chapter, different damage and/or defects in composite plate structures will be inspected and evaluated using a nonintrusive experimental setup of the PZT-SLDV Lamb wave inspection system. In addition, an automatic PL-SLDV system is developed and evaluated on a composite plate with simulated defects towards rapid NDE.

7.1 NON-INTRUSIVE PZT-SLDV SYSTEM SET UP

This section presents the non-intrusive experimental setup of the PZT-SLDV Lamb wave inspection system. The overall experimental setup of the PZT-SLDV system is given in Figure 7.1. A Steminc SM412 PZT[1] (0.5 mm thick and 7 mm diameter) is used for Lamb wave actuation, while the Polytech PSV-400-M2 SLDV system is employed for wavefield sensing. Traditionally, the PZT transducer is bonded on the surface with permanent adhesive as couplant, while reflective tapes are attached on the specimen surface for SLDV signal enhancement [62]. Removing the PZT transducer or the reflective tape are time consuming and may more or less adversely modify the material surface conditions. In order to implement truly nondestructive evaluation on the composite structures, non-intrusive setup is explored and implemented in this study, with selected honey (Simply Balanced from market[2]) as couplant for PZT actuation and wipe-off reflective spray (Albedo 100 reflective spray[3]) for SLDV measurement enhancement.

[1] https://www.steminc.com/PZT/en/
[2] https://www.target.com/p/organic-honey-16oz-simply-balanced-8482/-/A-53385493
[3] https://www.amazon.com/gp/product/B00WRNPI50/ref=ppx_yo_dt_b_search_asin_title?ie=UTF8&psc=1

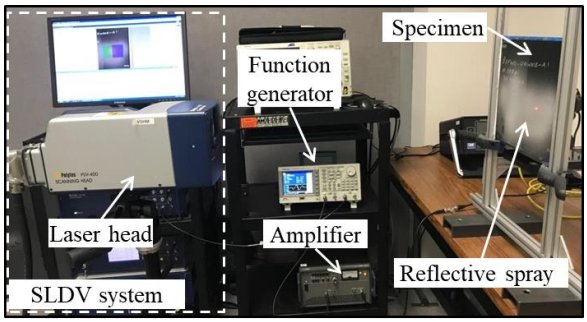

Figure 7.1 Experimental setup of the non-intrusive PZT-SLDV system [118]

The selected honey and wipe-off spray are shown in Figure 7.2a and Figure 7.2b respectively. To attach the PZT transducer, a syringe is used to apply a tiny drop of honey at the target surface and the PZT is then placed on top of the honey drop. Gentle thumb pressure is applied on the PZT transducer for two minutes so that the honey will distribute evenly between PZT and the specimen. The attached PZT is left for 24 hours before inspection so that the honey will be harden and cure. Figure 7.2c illustrates the PZT transducer attached on the surface with honey. Removable transparent tape is used to hold the wire in place on the plate (as shown in Figure 7.2c) to help the PZT stay on without sliding down if the specimen is placed vertically. On the other hand, the wipe-off reflective spray is applied with the spray nozzle being held 12 inches away and normal to the specimen surface as shown in Figure 7.2d. About 20 layers of spray is applied to the surface in order to achieve full signal level from the SLDV.

For Lamb wave inspection, 3-count Hanning window smoothed sinusoidal is used as excitation. It is generated by a function generator (Tektronix AFG3022C) at a selected frequency, magnified by an amplifier (NF HSA 4014), and then sent to the PZT actuator. Through in-plane piezoelectric coupling [96], Lamb waves are excited and propagate in the plates. Meanwhile through synchronization, the SLDV will simultaneously measure the multidimensional time-space Lamb wavefield over the desired scanning line or area. In

principle, SLDV measures velocity along its laser beam based on the Doppler frequency-shift effect on light waves. To obtain the out-of-plane Lamb wave velocity, therefore the SLDV head is placed normal to the specimen.

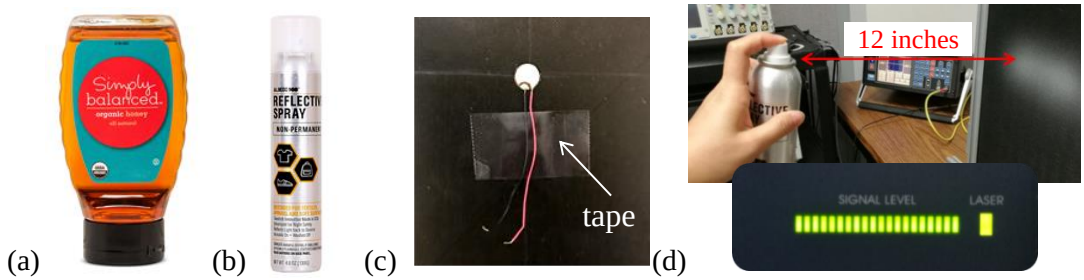

(a) (b) (c) (d)

Figure 7.2 Non-intrusive PZT-SLDV system setup: (a) Honey couplant by Simply Balanced, (b) wipe off reflective spray by Albedo 100, (c) PZT attached using honey as couplant. Transparent tape is used to hold the wire in place on the plate. and (d) spray applying illustration and related signal strength

7.2 WRINKLE DETECTION IN FLAT COMPOSITE PLATES

In this section, a flat laminated plate with wrinkle defects is inspected with a nonintrusive PZT-SLDV system. Multidimensional time-space wavefield data is acquired, and wave wrinkle interactions are observed. An adaptive wavefield imaging method is developed based on the time of flight of the first wave package of the acquired signal and applied to visualize and evaluate the wrinkle defect in the plate.

7.2.1 Evaluation method: adaptive wavefield imaging

Very often, directly acquired wavefield does immediately show the wave-defect interactions, indicating the existence of structural discontinuity [16, 17, 20, 55]. However, such detection requires experiences of wavefield analysis and immediate visualization of discontinuity in the structure is highly desired. Studies have shown that evaluating the wave energy along the wave propagating distance provides a rapid yet effective way to generate an inspection image of the plate [22, 25]. The wave energy can be represented by quantities

such as the peak amplitude or the root-mean-square value of the waveform at the position [119]. However, it has shown that the resolution of such images are limited and the revealed defect features are not clear enough for quantification purpose [119].

Due to the multimodal property of Lamb wave [44] there are always at least two modes existing in the propagation. They usually travel at largely different velocities, resulting in a faster wave packet arriving first than other slower ones. The first arrival will yield clearer interaction features since it is less likely complicated by the slower modes or boundary reflections [119]. In this research, an adaptive wavefield imaging method has been developed that employs the first arrival for the evaluation of wrinkle defects in the flat composite panel. Assume the group velocity c_g of such a first arrival is known, its time of flight at a point (x,y) of interest in the plate can be determined as:

$$t_{tof}(\mathbf{x}) = \frac{\left|\sqrt{\left(x - x_0\right)^2 + \left(y - y_0\right)^2}\right|}{c_g} \tag{7.1}$$

where (x_0,y_0) is the location of excitation source. Using the calculated $t_{tof}(\mathbf{x})$, the first arrival of the acquired wave can be retained through a windowing technique. The window $W_{t_{tof}}(t)$ is defined with its center at $t_{tof}(\mathbf{x})$ and having a width of double length of the excitation signal. The window is then applied to the wavefield as:

$$v_{1\text{st}}(t, \mathbf{x}) = v(t, \mathbf{x}) W_{tof}(t) \tag{7.2}$$

In this study, a Tukey window [120] is used since it offers a "flat top" to offer unit gain within the interested time frame of first arrival signals. Using the windowed first arrival, an intensity image based on the amplitude information is then generated to indicate the presence of the defect as well as its locationas:

$$v_{1\text{st}}^{mag}(t, \mathbf{x}) = \max\left|v_{1\text{st}}(t, \mathbf{x})\right| \tag{7.3}$$

7.2.2 Actuation and sensing setup

The flat composite plate is manufactured with total 20 plies and 3.83 mm thickness. The overall dimension of the plate is measured at 306 × 260 (unit: mm). Significant wrinkles can be observed on both top and bottom surfaces, as illustrated in Figure 7.3a (indicated by the arrows), and also can be seen from the side along the thickness direction as in Figure 7.3b. No other information of this wrinkle plate is available such as the material properties as well as the detailed layup. To assist the inspection, Cartesian coordinates are employed with the origin set at the left bottom corner of the plate. We have chosen to study the area with more visible wrinkles and referred it as "wrinkle region", in contrast to the area with less visible wrinkles as "reference region", as shown in Figure 7.3c. A PZT actuator is placed at location (160, 110) on the specimen (Figure 7.3c) to excite the waves. Area scans (95 mm by 60 mm) are performed on both the top and bottom surfaces in the wrinkle region, using the area scan setup given in Figure 7.3c. Line scan within the reference area has also been performed for dispersion curve acquisition and inspection parameter setup. The SLDV scanning spatial resolution is 1 mm and the sampling rate is 10.24 MHz.

Before inspection, Lamb wave dispersion curves along x axis on both sides are acquired experimentally through line scan (10 to 100 mm from the PZT) in the reference region for better understanding of the excited Lamb wave modes in the target plate. The detailed process can be found in Section 3.4. The results are plotted in Figure 7.4. One can see that there is no significant difference between the dispersion curve results obtained on the top and bottom surface. In addition, only two modes exist in the frequency range below 400 kHz, and more modes are observed in the higher frequency range.

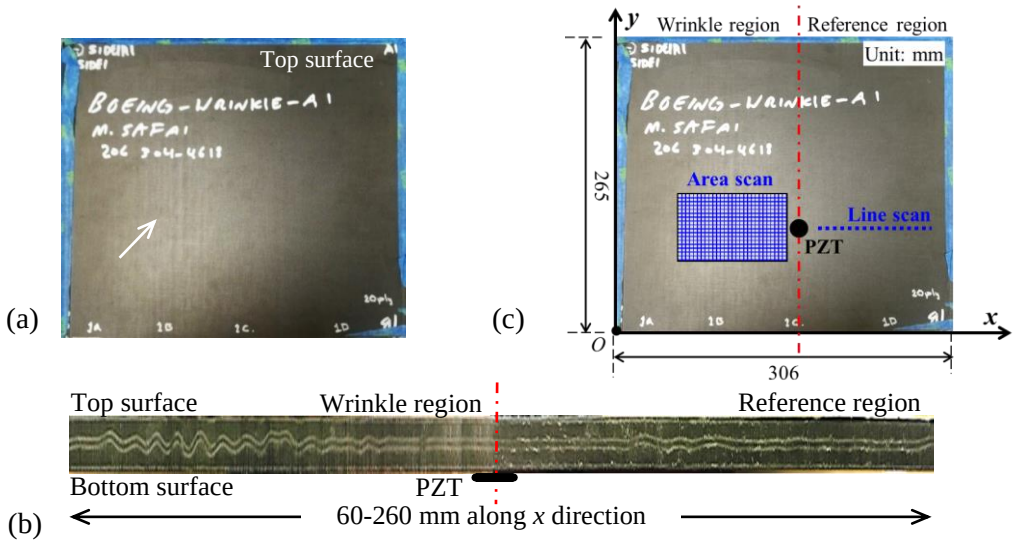

Figure 7.3 Inspection of composite plate with wrinkle defect: (a) top surface, (b) side view, and (c) actuation and sensing schematic

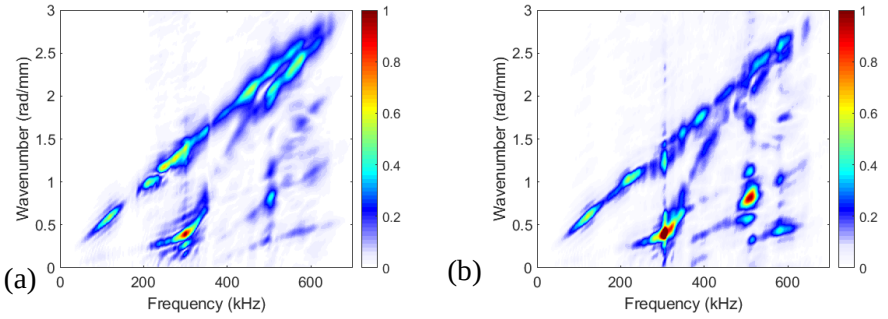

Figure 7.4 Experimental frequency-wavenumber dispersion curve acquired on: (a) top surface, and (b) bottom surface

For Lamb waves NDE, as frequencies go higher, more wave modes are likely to be excited and cause complexity in subsequent damage evaluation. Therefore, low frequency is often employed [33]. Two quick wave acquisition through line scans (Figure 7.3c) to identify a proper excitation frequency are first performed in the reference region. The scans are along *x* axis from 10 to 100 mm away from the PZT actuator at 120 kHz and 210 kHz. The acquired time-space wavefield as well as a waveform at a certain propagating distance are presented in Figure 7.5 for both frequencies. From Figure 7.5a, we can see that there are

two wave packets in the 120 kHz Lamb waves but the first arrival at about 30 μs has very weak strength. On the other side, the first arrival of the waves at 210 kHz in Figure 7.5b exhibits much stronger strength and will be ideal for the wrinkle inspection since we are set to use the first arrival as stated in section 3.1. Thus, 210 kHz will be used as the excitation frequency for the inspection in the wrinkle plates.

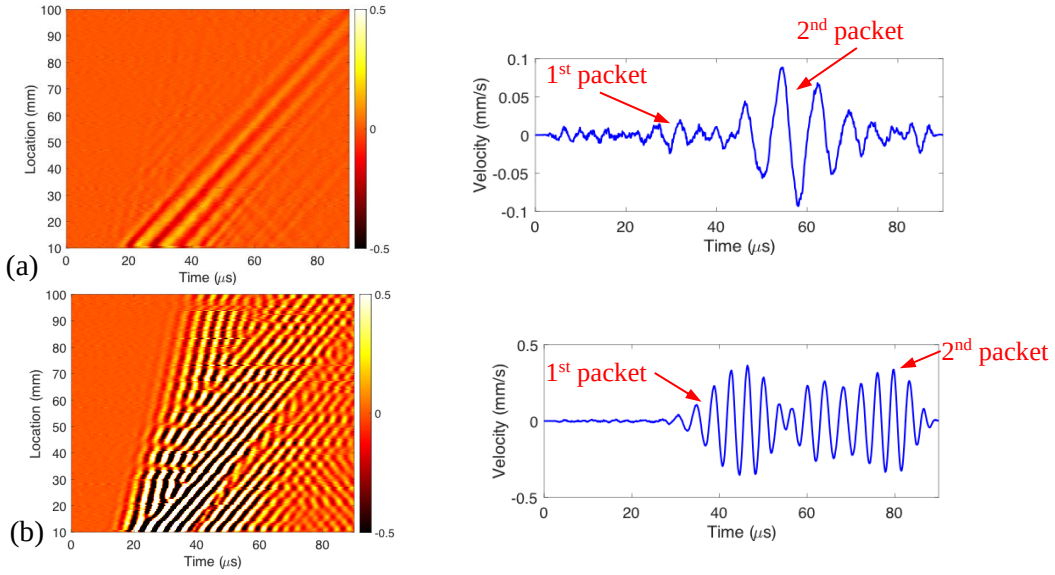

Figure 7.5 Line inspection results: (a) time-space wavefield at 120 kHz, and representative waveform at 50 mm, and (b) time-space wavefield at 210 kHz, and representative waveform at 85 mm

To implement the imaging algorithm, the group velocity of the first arrival in the acquired waves at 210 kHz needs to be determined by finding out its time of flight (TOF) at a given propagation distance. To estimate the group velocity more accurately, eleven signals from 70 to 90 mm at a 2 mm increment along the scanning line are used. Three example waveforms at propagating distance 70, 80, and 90 mm are plotted in a. Hilbert transform is applied to extract the envelops of these waveforms and the TOFs of the first arrivals are extracted indicated by the peak arrival time (e.g. TOF is 47.5 μs at 90 mm in Figure 7.6a). All of the acquired TOF and corresponding propagating distance are plotted in Figure 7.6b

(blue stars). The plot shows a linear relationship which can be curved fitted through linear regression (red line, derived with linear curve fitting as $y = 5.249x - 158.23$). The group velocity of the first arrival is therefore obtained, which is about 5.249 mm/μs.

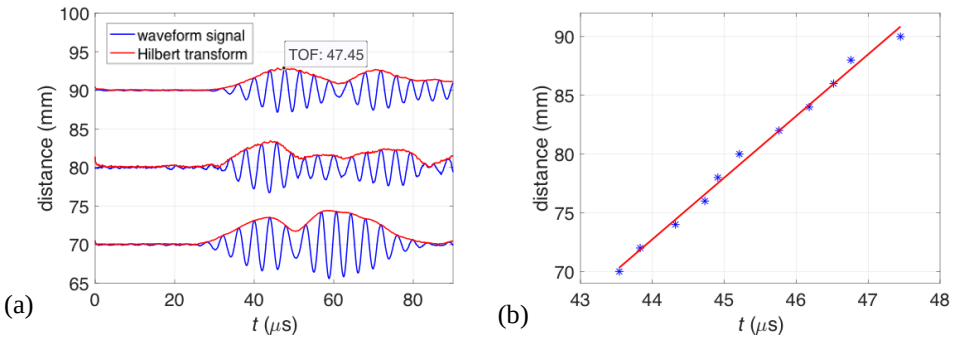

Figure 7.6 Group velocity estimation of the first arrival: (a) waterfall plots of representative waveforms (70-90 μs) used for the group velocity estimation, and (b) linear regression result showing c_g is about 5.249 mm/μs (the slope)

7.2.3 Evaluation results

Inspection using the subject PZT-SLDV system is performed on the wrinkle region on both top and bottom surfaces of the test plate using the setup given in Figure 7.3c. The resulted time-space wavefields are presented in Figure 7.7. Circular wavefront can be observed in the incident waves leaving the PZT actuator for both results. The circular wavefronts then changed to straight crest ones when they arrived at and passed through the wrinkles. Comparing the waves measured on the top (Figure 7.7a) and bottom (Figure 7.7a), the wave interaction with defects are occurring in similar range (90 to 130 mm along x direction). It matches with the visually observed wrinkle range in the plate. The detection of wrinkles from both top and bottom indicates the wrinkles might be manufactured through the thickness and can be inspected from either side.

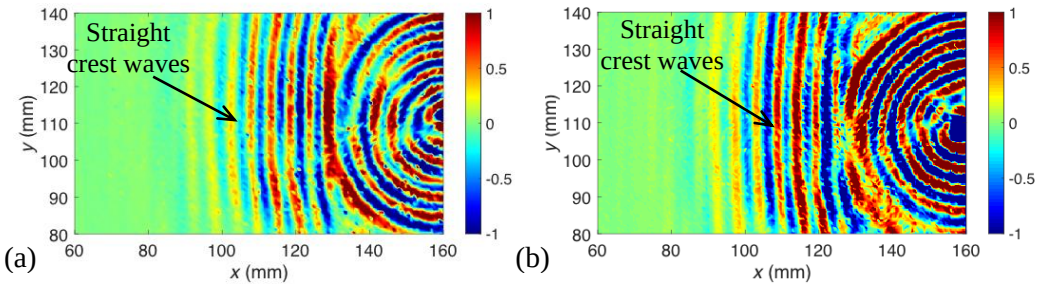

Figure 7.7 Wavefield results at 29 μs of the wrinkle region measured on: (a) top surface, and (b) bottom surface, both showing incident circular crest waves change to straight crest waves

The wavefield data have been further processed with the adaptive wavefield imaging method outlined in section 3.1 and the results are given in Figure 7.8a and Figure 7.8c for top and bottom surface respectively. It can be observed that the wave energy has two distinguish distributions in the range 80 to 130 mm and 130 to 160 mm in both images. In the range 130 to 160 mm, the strong energy from the incident waves are observed with a circular shape. While in the range 80 to 130 mm, strip shaped wave energy distribution is observed. The zoom in images of the wrinkle range are presented in Figure 7.8b and Figure 7.8d for top and bottom surface respectively. Clear wrinkle patterns are visualized now with peak and valleys represented by the blue and red color in both images. The wrinkle patterns are discernibly visualized in both images within the range 80-130 mm along *x* direction, and the identified wrinkle ranges agree well with that observed through visual examination given in Figure 7.3b.

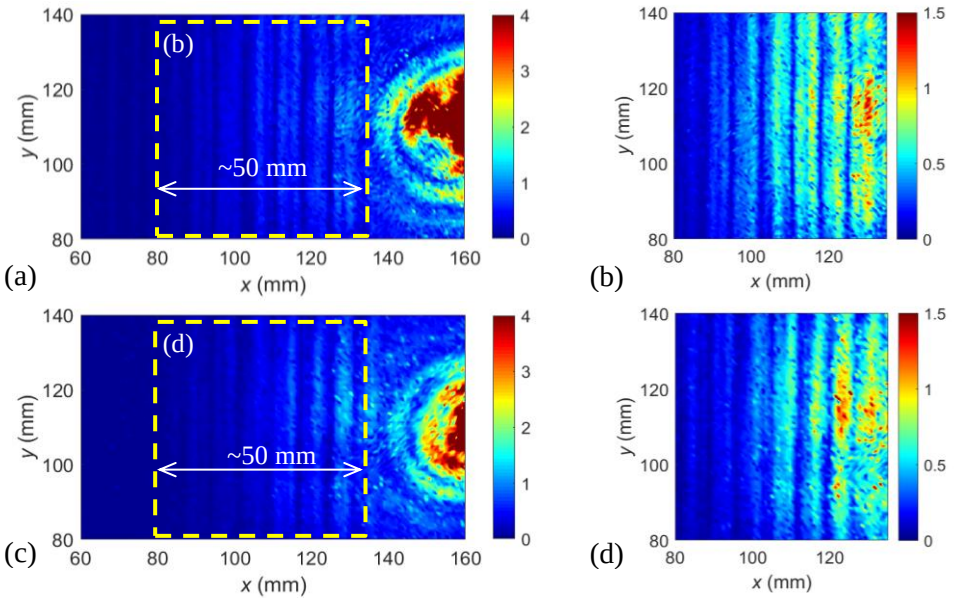

Figure 7.8 Wrinkle defect evaluation using adaptive wavefield imaging method. Images obtained on (a) top surface and (c) bottom surface. Zoom in images of the wrinkle defects on (b) top surface and (d) bottom surface

7.3 DELAMINATION DETECTION IN A CURVED COMPOSITE PLATE

In this section, three curved composite plates with different curvature are inspected using the nonintrusive PZT-SLDV system. Wavefield data are acquired and wave-delamination interaction are observed. The wavefield data are further processed with weighted sum wavenumber imaging method presented in Section 4.3.2 and the delaminations are highlighted in all the tested plates.

7.3.1 NASA-RP-40D

This curved composite plate named NASA-RP-40D is manufactured with embedded delamination in between different layers. The top surface and side view of the curved plate are shown in Figure 7.9a and Figure 7.9b respectively. The plate measures about 101 mm high and 7 mm thick, and 160 mm top surface arc length. Two area inspections are performed on each surface of the plate with one for the wing W1 and another for W2 as shown in Figure 7.9c. A 3-count toneburst amplified to 50 Vpp is used as excitation for

each inspection. The excitations are located at the center of each wing, O_1 for W1 and O_2 for W2, so that the wave propagation can cover that the entire wing. Inspection frequency evaluation similar to that given in Section 7.2 is performed, and 150 kHz is selected as it provides strong wave-defect interaction. The SLDV head is placed normal to the surface where the excitation is located as shown in Figure 7.9d. Due to the curvature of the plate, the SLDV will not maintain normal to the plate surface of the whole scan area, as illustrated in Figure 7.9d. Such scanning angle effect and resulted loss in wave strength are not considered in this study since our study goal is to explore if the present measurement and analysis methods are applicable for delamination detection on plates with such amount of curvature. For each inspection, the scanning area covers the accessible surface of the inspected wing: around 90 mm × 90 mm within *x*-*y* plane. The SLDV spatial resolution is 1 mm and the sampling rate is 10.24 MHz. Note the inspection area on top and bottom surface differs subtlety due to the plate curvature.

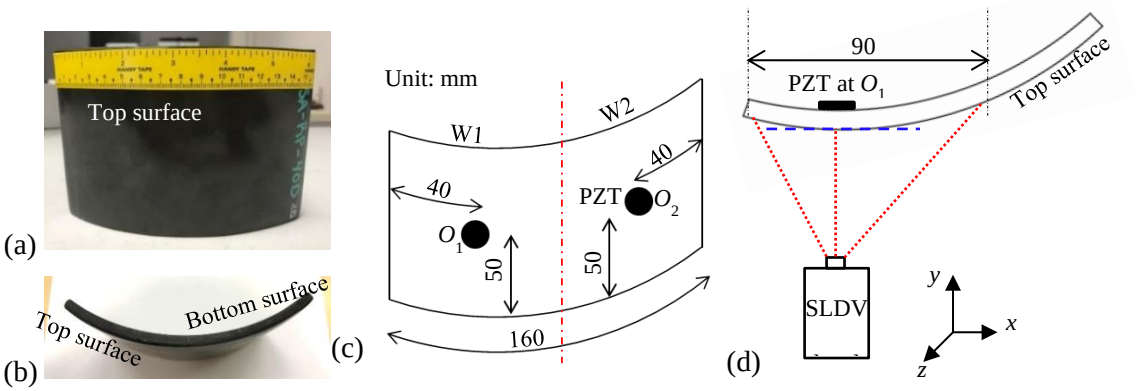

Figure 7.9 Inspection of NASA-RP-40D: (a) top surface view, (b) side view showing the curvature, (c) actuation locations for W1 and W2 inspection, (d) actuation and sensing schematic for W1 inspection on the top surface with PZT at O_1

Figure 7.10a and Figure 7.10b plot the wavefield snapshots at 45 μs for W1 and W2 inspection on the top surface. The wave-delamination interactions can be immediately

noticed at two locations along y=50 mm (marked as D2) and 82 mm (marked as D1) from the wavefield plots. Similar wave-defect interactions are observed: (a) defect induced waves at D1 as shown in Figure 7.10d with significantly smaller wavelength compared to the 10 mm nominal wavelength of the incident waves (Figure 7.10c); (b) defect induced waves at D2 (Figure 7.10e) with obvious higher intensity while no obvious wavelength change compared to the incident waves (Figure 7.10e) indicating possibility of presence of defect.

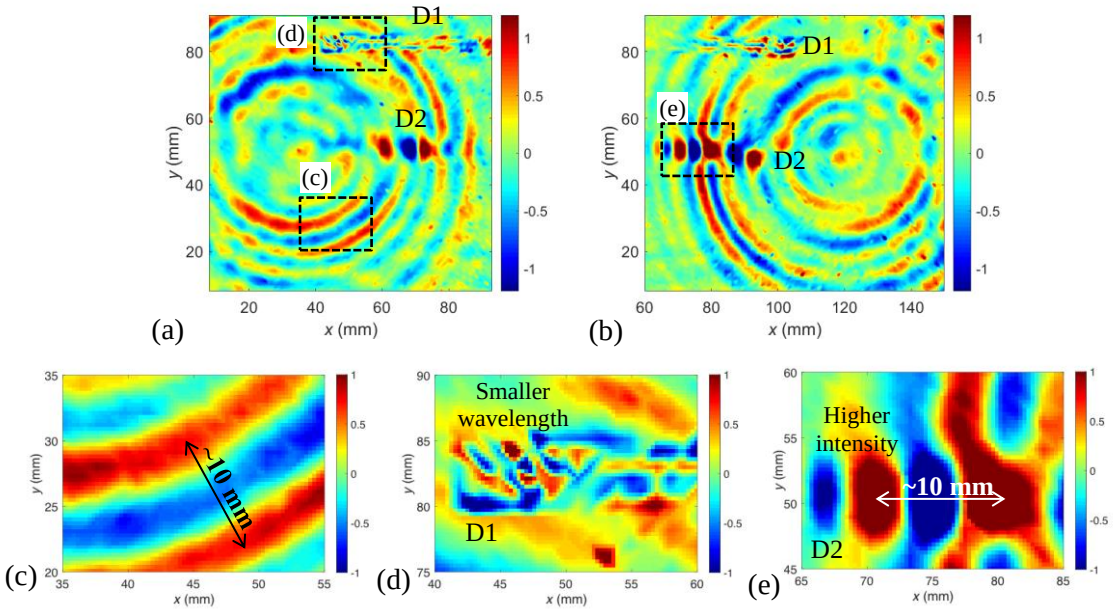

Figure 7.10 Damage evaluation of the curved plate: wavefield snap shot at 45 μs on top surface of (a) W1, and (b) W2; wavenumber imaging results on top surface (c) W1, and (d) W2

Further evaluation of the delamination in the curved plate is conducted with the weighted wavenumber imaging method given in section 4.1. The resulted wavenumber images are plotted in Figure 7.11a and Figure 7.11b. From the image for W1 (Figure 7.11c), a strip shaped defect (D1) is highlighted with large wavenumbers in the range 40 mm to 90 mm along *y*=82 mm, which is consistent with the shorter wavelength observed in the wavefield snapshot (d) given the inverse relationship between wavenumber and wavelength [16]. In

addition, another strip like defect (D2) can also be observed in the range x=40-90 mm at y=50 mm through the indication via slightly wavenumber variations, which is consistent with the wavefield observation that no obvious wavelength change (Figure 7.10e). In the wavenumber image for W2 (Figure 7.11b), D1 (y=80 mm) and D2 (y=50 mm) are indicated in the range 60 mm to 110 mm along x axis. By comparing the imaging results of W1 and W2, we can conclude that D1 and D2 are localized in the range 40 mm to 110 mm along x axis with D1 at 82 mm and D2 at 50 mm along y axis.

The inspection wavenumber imaging results obtained on bottom surface are presented in Figure 7.11c and Figure 7.11d. Similar subtle wavenumber variation are observed at the D2 location detected earlier on the top surface, which further confirms the D2 range and shape. In addition, another strip shaped defect (D3) is observed, located at y=18 mm with similar range along x axis, 40-110 mm by considering both the results of Figure 7.11c and Figure 7.11d. Through comparing the inspection results on top and bottom surface, we can conclude that: (1) three strip shape defect exist in the plate in the range about 40 mm to 110 mm along the x axis with D1 at 82 mm, D2 at 50 mm and D3 at 18 mm along y axis, and (2) along the thickness direction, D1 is close to top surface since it is only clearly highlighted in the results obtained on the top surface, while D3 is close to the bottom surface since it is only visualized in the results measured on the bottom surface. D2 shall be located within the middle plane since the interaction is more difficult to capture on both surfaces resulting in lower imaging resolution.

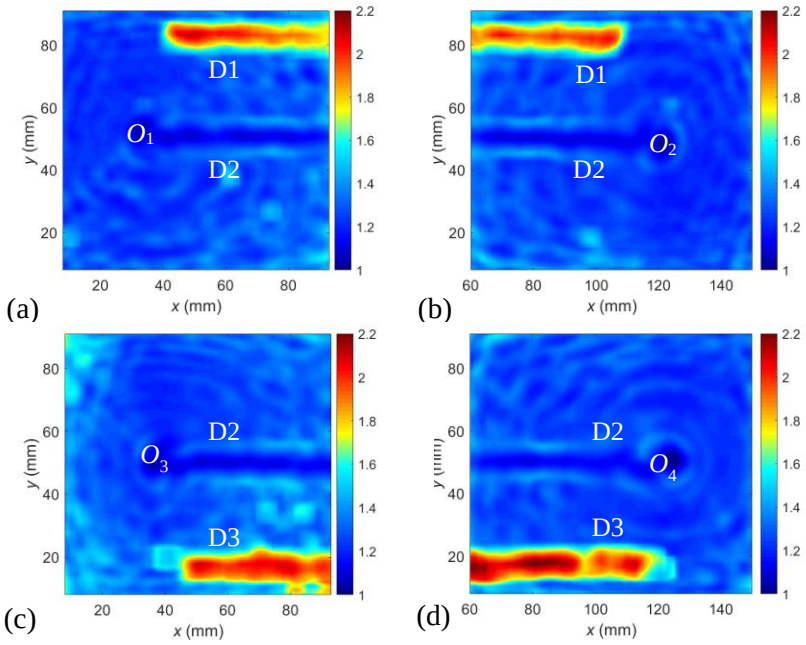

Figure 7.11 Wavenumber imaging obtained on the bottom surface: (a) W1, and (b) W2

7.3.2 NASA-RP-20D

The inspection procedure is similar to that in last section. The inspection setup is illustrated in the Figure 7.12. Figure 7.12a shows the top view and Figure 7.12b shows the side view of the plate. The radius of curvature of the plate is 20 mm. The height of the specimen is 101 mm, and the thickness is around 7 mm. The length of the specimen outside surface is about 140 mm. The actuator is attached at O_1 and O_2 in order to inspect the specimen from different views. No other information about 20D is available to the inspectors. 2D area inspection is performed with actuation locations at O_1 and O_2 on both sides as illustrated in Figure 7.12c. For each inspection, the scanning area covers the accessible surface of the specimen: around 90 mm × 90 mm for both sides. For each side, the inspection area differs a little due to the curvature. Note that the scanning area is not identical to the real curved surface, and the measured wavefield is the shrink version of original wavefield in *x*-*z* plane due to the curvature. The SLDV head is placed as shown in Figure 7.12d, and the scanning

angle effect is not considered. The remaining experimental setup keeps the same as in Section 7.2.1.

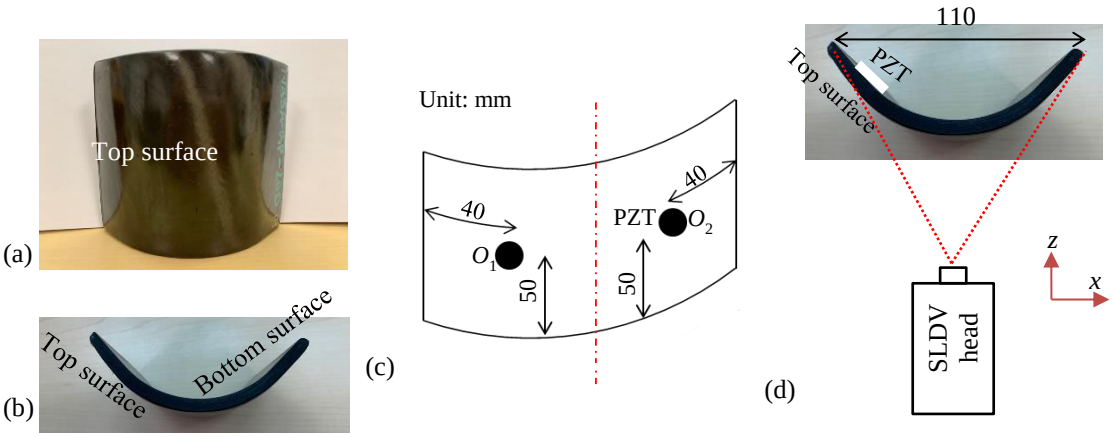

Figure 7.12 Inspection setup of NASA-RP-20D: (a) top surface view, (b) side view showing the curvature, (c) actuation locations for the inspection, (d) actuation and sensing schematic on the top surface with PZT at O_1

The wavenumber imaging process are performed for the measured wavefields and the results are presented in Figure 7.13 and Figure 7.14 for the top and bottom surface respectively. The imaging results on the top surface with PZT at O_1 (Figure 7.13a) and with PZT at O_2 (Figure 7.13b) shows consistency. A strip shape damage (D1) is observed in the range 70 mm to 80 mm along x direction at y=80 mm. In addition, another damage D2 is observed at y=50 mm while its shape and range cannot be distinguished. The wavenumber imaging results obtained on bottom surface presented in Figure 7.14 shows consistency as well with the two excitation locations. Three strip-like shape damage D3, D4, and D5 are observed at y=20 mm in the range 15-25 mm, 30-50 mm, and 85-90 mm along x axis respectively. Through comparing the inspection results on top and bottom surface, we can conclude that: (1) Five strip shape damage exist in the plate with D1 at 80 mm, D2 at 50 mm and D3, D4, and D5 at 20 mm along y axis, and (2) In the thickness direction, D1 is

close to top surface, D2 is located in the middle, and D3, D4, and D5 are close to the bottom surface.

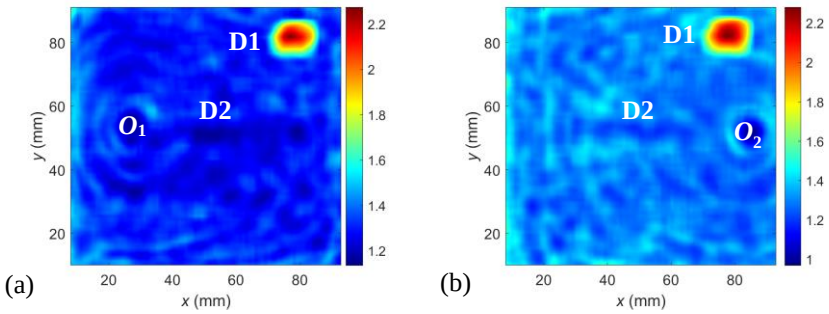

Figure 7.13 Wavenumber imaging obtained on the top surface: (a) with PZT at O_1, and (b) with PZT at O_2

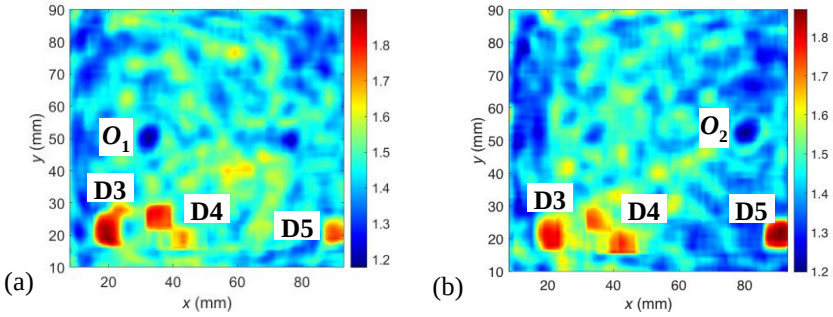

Figure 7.14 Wavenumber imaging obtained on the bottom surface: (a) with PZT at O_1, and (b) with PZT at O_2

7.3.3 NASA-RP-10D

The inspection setup is illustrated in the Figure 7.15, with Figure 7.15a for the top view and Figure 7.15b for the side view of the plate. The radius of curvature of the plate is 10 mm. The height of the specimen is 101 mm, and the thickness is around 7.28 mm. The length between the specimen edge is 110 mm. The actuator is attached at O_1 and O_2 in order to inspect the specimen from different views. No other information about this plate is available to the inspectors. 2D area inspection is performed with actuation locations at O_1 and O_2 on both sides as illustrated in Figure 7.15c. For each inspection, the scanning area covers the accessible surface of the specimen: around 90 mm × 90 mm for both sides. For

each side, the inspection area differs a little due to the curvature. Note that the scanning area is not identical to the real curved surface, and the measured wavefield is the shrink version of original wavefield in *x*-*z* plane due to the curvature. The SLDV head is placed as shown in Figure 7.15d, and the scanning angle effect is not considered. The remaining experimental setup keeps the same as in Section 7.2.1.

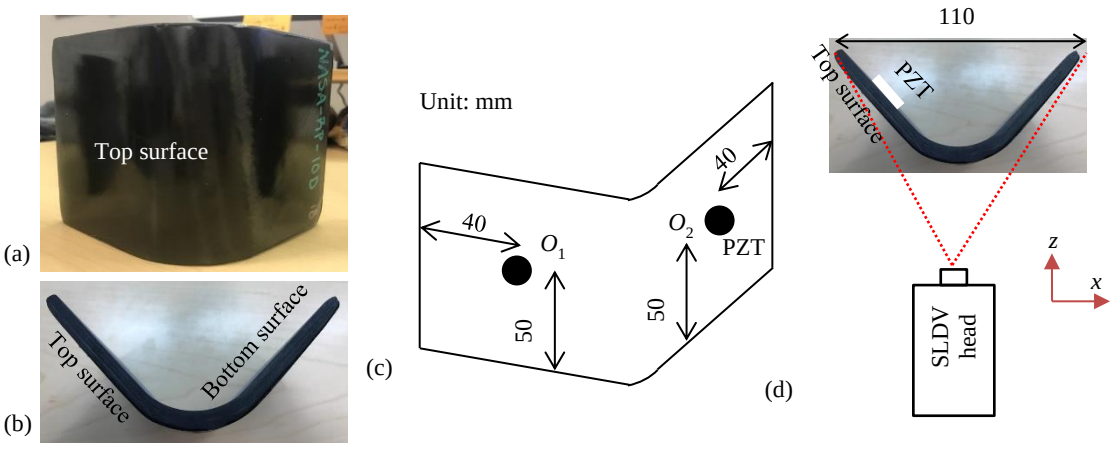

Figure 7.15 Inspection setup of NASA-RP-10D: (a) top surface view, (b) side view showing the curvature, (c) actuation locations for the inspection, (d) actuation and sensing schematic on the top surface with PZT at O_1

The wavenumber imaging process are performed for the measured wavefields and the results are presented in Figure 7.16 and Figure 7.17 for the top and bottom surface respectively. The imaging results on the top surface with PZT at O_1 (Figure 7.16a) and PZT at O_2 (Figure 7.16b) agree well with each other. A strip shape damage (D1) is observed in the range 45 mm to 70 mm along *x* direction at *y*=80 mm. In addition, another damage D2 is observed at *y*=50 mm while its shape and range cannot be distinguished. The wavenumber imaging results obtained on bottom surface presented in Figure 7.17 shows consistency as well with the two excitation locations. One strip-like shape damage D3 are observed at *y*=20 mm in the range 45-70 mm, and another circular damage is seen in the

range 90-95 mm. Through comparing and combining the inspection results on top and bottom surface, we can conclude that: (1) Four damage exist in the plate with D1 at 80 mm, D2 at 50 mm and D3 and D4 at 20 mm along *y* axis, and (2) In the thickness direction, D1 is close to top surface, D2 is located in the middle, and D3 and D4 are close to the bottom surface.

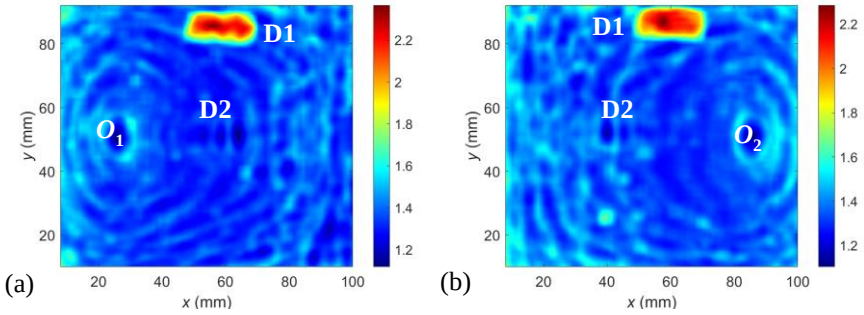

Figure 7.16 Wavenumber imaging obtained on the top surface: (a) with PZT at O_1, and (b) with PZT at O_2

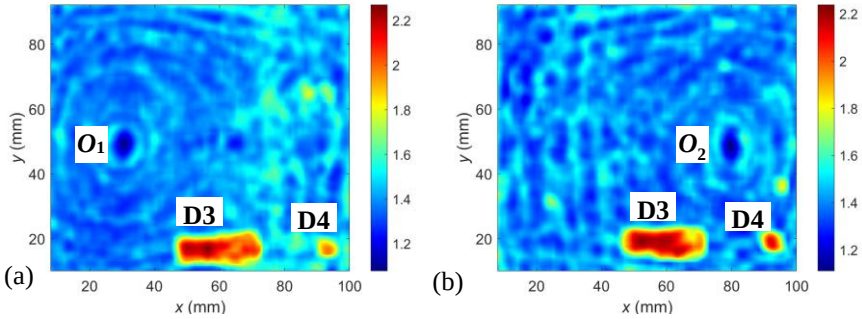

Figure 7.17 Wavenumber imaging obtained on the bottom surface: (a) with PZT at O_1, and (b) with PZT at O_2

In this section, three curved composite plates with different curvature are inspected using the non-intrusive PZT-SLDV system and the delamination are visualized with the weighted wavenumber imaging method. Since the system measures the surface particle velocity, the delamination close to the scanning surface will have the highest intensity. Through inspection on both top and bottom surfaces, the delamination close to the two surfaces are highlighted. While the delamination close to the middle layer of the plate is not visualized

as clear as the ones close to the surface. Although the three different plates have different curvature, the SLDV 2D measurement (projection) in terms of space without considering the angle effect successfully detected and visualized the delamination.

7.4 PILLOW LIKE DEFECT EVALUATION IN THICK COMPOSITES

In this section, a thick composite plate with pillow defects are inspected using the non-intrusive PZT-SLDV system. Wavefield data are acquired with PZT attached at different locations to cover the whole plate. Wave-defect interaction are observed in all the wavefield snapshots: waves with smaller wavelength trapped in the defect area. The wavefield data are further processed with maximum intensity wavenumber imaging method and all the defects are highlighted and visualized.

7.4.1 Experimental setup

The top and bottom view of specimen UTC-3 are shown in Figure 7.18a and Figure 7.18b. The size of the specimen is 335 mm by 335 mm, and the thickness is around 13.3 mm. Ten pillow defects are observed with 5 being closer to top surface and 5 being closer to bottom surface as pointed in yellow arrow. The size of the defects increases from up edge to bottom edge of the specimen. No other information about UTC-3 is available to the inspectors. The non-intrusive PZT-SLDV system is used for the inspection. A 3-count toneburst at 180 kHz amplified to 100 V_{pp} is used as excitation. In order to cover the whole plate, the inspection is performed through three area scans with three different excitation locations as shown in Figure 7.18c. Cartesian coordinates are employed (unit: mm), and the coordinates of the three actuation locations for top surface are AC-1 to AC-3 are (110,90), (110,200), and (110,245). The area scan spatial resolution is 1 mm. The same setup is

adopted for bottom surface except the excitation locations for AC-1 to AC-3 are (225, 90), (225, 200), and (225, 245) respectively.

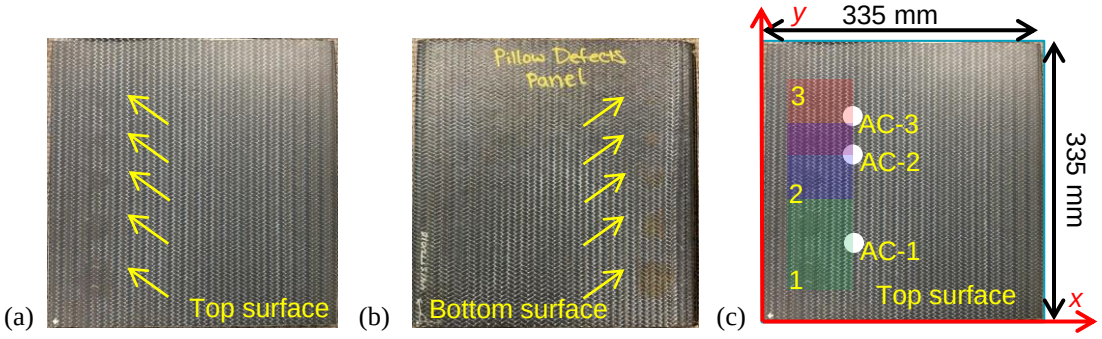

Figure 7.18 Experimental setup: (a) PZT-SLDV system, and (b) actuation and sensing schematic

7.4.2 Inspection results on top surface

The time-space wavefield of the three scanning area are plotted in Figure 7.19(b)-(d) respectively. One can see that strong wave interactions appeared in the defect area in all the wavefield results. Some waves trapped in the defect area when the waves encounter the defect and the trapped waves have shorter wavelength. Five defects are highlighted in the wavefields and their shape are circular. To better visualize the defects, wavenumber images are generated using the methodology in Section 4.3.2 and plotted in Figure 7.19(e)-(g) respectively. It can be observed that all the defects are highlighted clearly with high wavenumber, which is corresponding to the trapped waves with shorter wavelength. The defects are all in circular shape as observed in the wavefield snapshots and the defect diameters are estimated from the wavenumber images as 38 mm, 25 mm, 19 mm, 13 mm, 6 mm respectively.

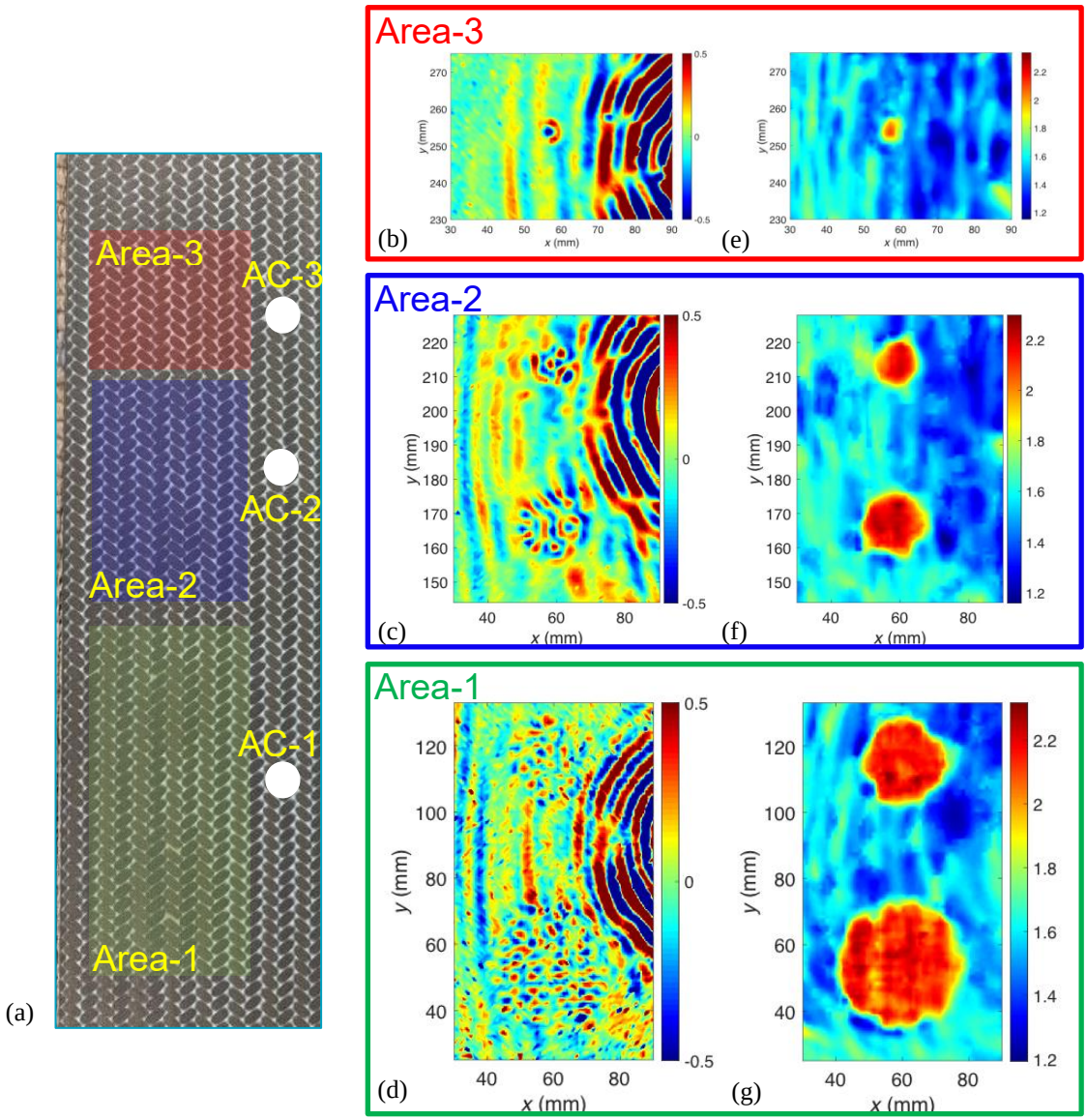

Figure 7.19 Top surface inspection results: (a) actuation and sensing setup, (b)-(d), wavefield snapshot to show wave interaction with defects, and (e)-(g) wavenumber imaging results of different scanning areas

7.4.3 Inspection results on bottom surface

The time-space wavefield of the three scanning area on the bottom surface are plotted in Figure 7.20(b)-(d) respectively. Trapped waves with shorter wavelength are observed for four defects (larger sizes). Wave interaction was not observed for the smallest defect which can be seen from the visual inspection. Wavenumber images are generated and plotted in

Figure 7.20 (e)-(g) respectively. Part of the smallest defect showed up in the wavenumber image as shown in Figure 7.20 (e). The other four larger defects' shape are all circular, and their diameters are estimated from the plots as 38 mm, 25 mm, 19 mm, 13 mm respectively. In summary, total of ten defects are detected in this plate and most of their shape are circular.

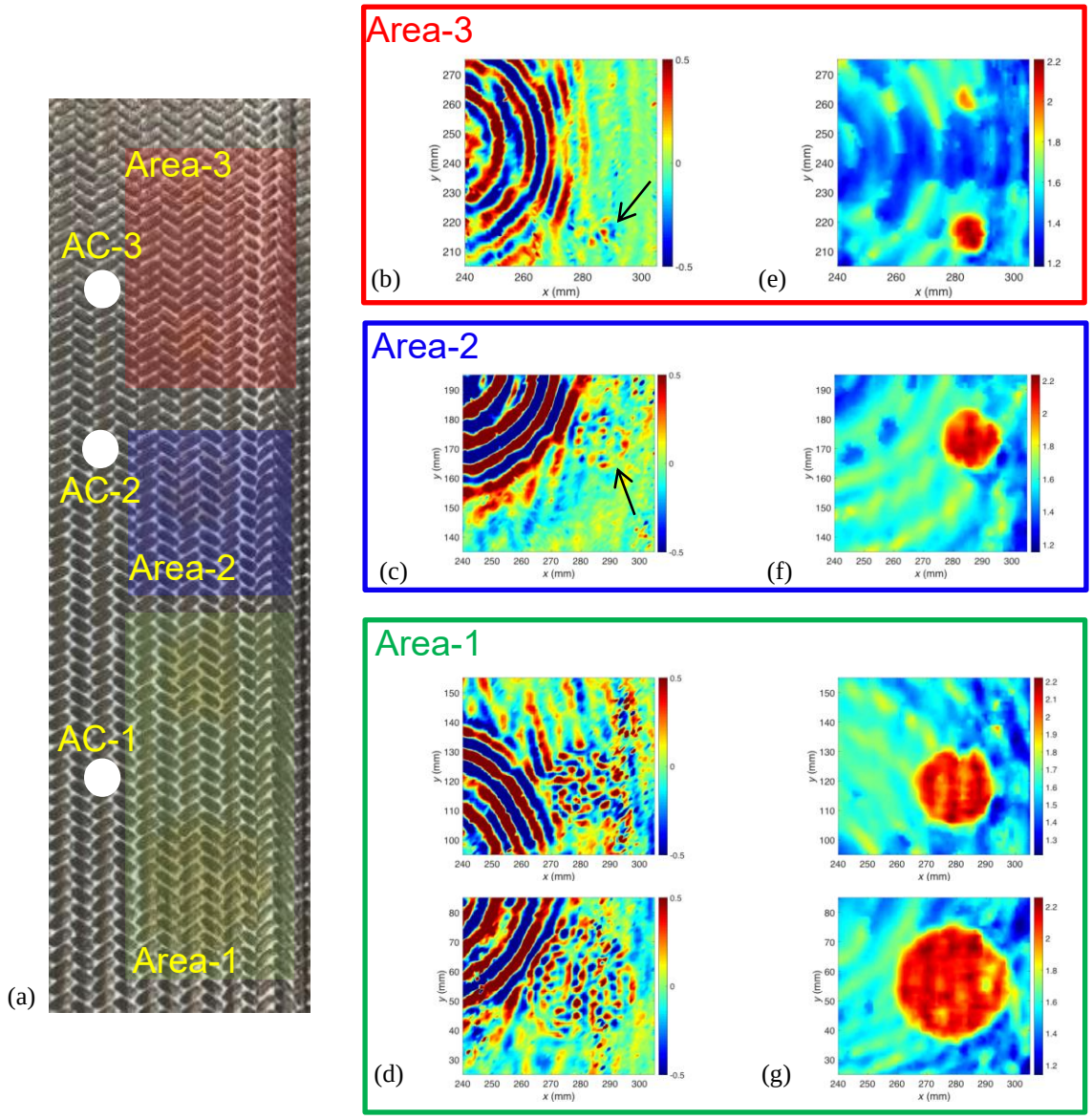

Figure 7.20 Bottom surface inspection results: (a) actuation and sensing setup, (b)-(d), wavefield snapshot to show wave interaction with defects, and (e)-(g) wavenumber imaging results of different scanning areas

7.5 AUTOMATIC PL ACTUATION ON A COMPOSITE PLATE

The automatic pulsed laser actuation which can excite Lamb waves on any desired location flexibly is explored in this section to enable rapid NDE inspection during manufacturing process of composite structures or any their service time. The PL-SLDV NDE system presented previously in Chapter 5, where the PL is fixed on the experiment table, can only excite Lamb waves at a fixed location. Toward automatic PL-SLDV NDE system, the PL head is mounted on an industrial KUKA robotic arm in order to enable the PL excitation movement. The system layout of the robotic PL-SLDV NDE system is shown in Figure 7.21, where the PL head movement is controlled by the KUKA arm.

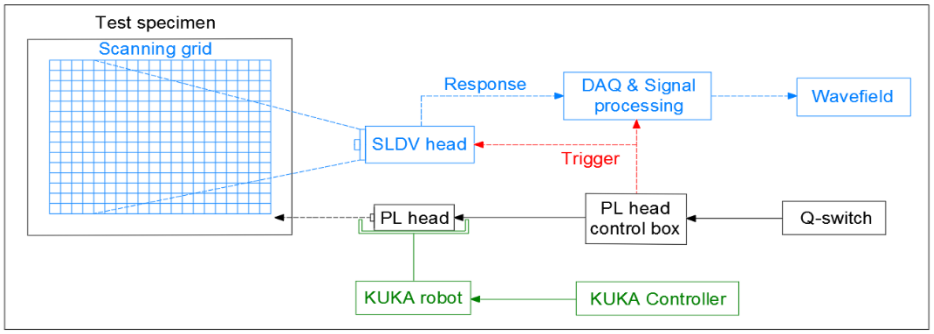

Figure 7.21 System layout of the robotic PL-SLDV NDE system [100]

7.5.1 Experimental setup

A KR6 R700 sixx KUKA robot[4] is selected to enable the PL movement. The maximum payload of this robotic arm is 6 kg, which is larger than total weight of the PL head (3 kg). The mounting illustration is shown in Figure 7.22a. In order to mount the PL laser head on the KUKA arm, a 2 mm thick aluminum mounting adapter is manufactured. Seven M5-0.8×8 socket head cap screws are used to attach the adapter to the KUKA arm mounting flange. A 9 mm thick wood spacer is mounted on the adapter. The PL laser head is mounted

[4] KR AGILUS sixx with W and C Variants Specification

on the spacer and then tightened with 3 M4-0.7 × 35 screws and M4-0.7 hex nuts. Figure 7.22b shows the PL head mounted on the KUKA arm and ready for excitation. The overall experimental setup of the robotic PL-SLDV NDE system is shown in Figure 7.23a. KUKA SmartPad is used to control the KUKA arm and enable the PL movement. Since the laser output beam is invisible, two class I line lasers (one is set up as horizontal and the other as vertical w.r.t. the laser source) are used for the alignment as shown in Figure 7.23b. An example of positioning PL excitation point using the alignments lasers is illustrated in Figure 7.23c. In addition, a camera (Figure 7.23d) connected to the PC is used to monitoring the inspection process and ensure the desired PL movement. Other settings keep the same as the fixed PL-SLDV system setup.

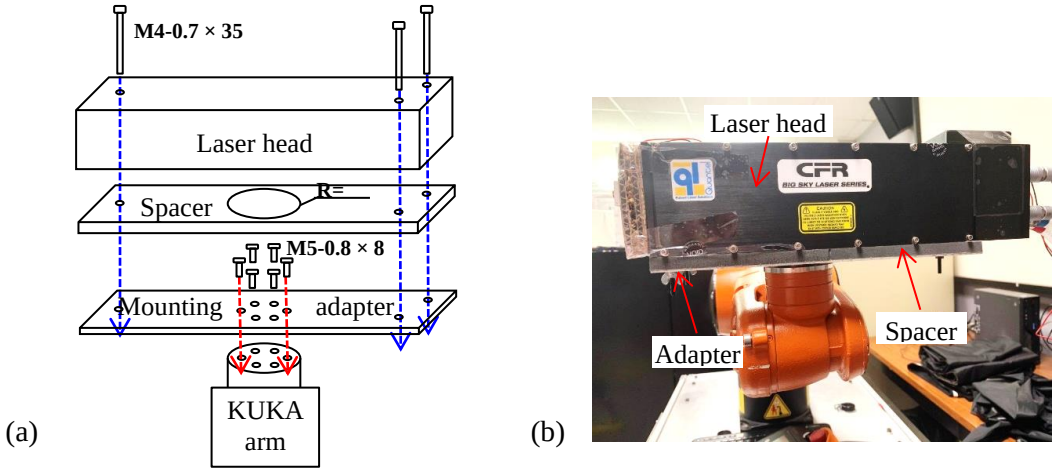

Figure 7.22 PL installation on the KUKA arm: (a) detailed schematic of the mounting process, and (b) PL laser mounted on KUKA arm

For proof of concept study, four locations (PL-1, PL-2, PL-3, and PL-4) on a composite plate are selected as target point of PL excitation as shown in Figure 7.24. The composite plate is a 8-ply quasi-isotropic plate with layup $[0/45/90/-45]_s$. The composite plate has a 10 mm circular quartz bonded as a simulated damage at the center, which is defined as the origin of the coordinates. With each PL excitation, the SLDV will perform a quick line

scan for 1D inspection (Figure 7.24a) and a more detailed area scan for 2D inspection (Figure 7.24b) simultaneously. The line scans are from 10 to 100 mm away from the PL excitation point. The area scans are about 50 mm by 50 mm. The spatial resolution is 0.5 mm for both inspections.

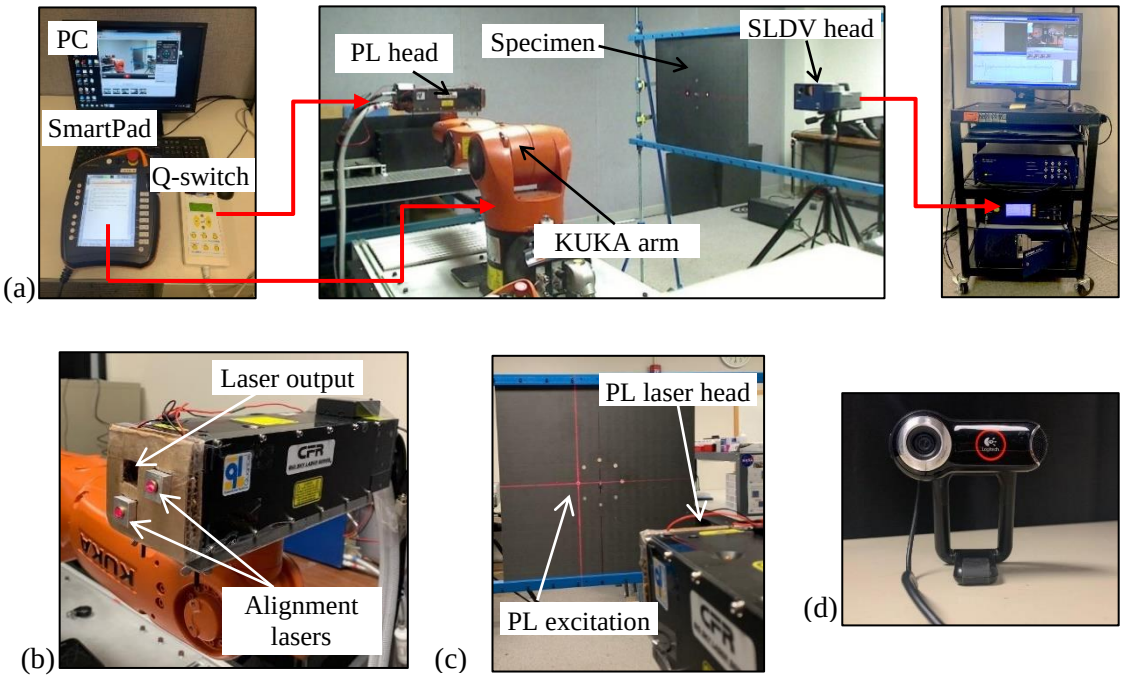

Figure 7.23 Experimental setup of the robotic PL-SLDV NDE system: (a) overall experimental setup, (b) monitoring camera, (c) alignment line-lasers mounted on the PL head, and (d) alignment line-lasers positioning the PL excitation point

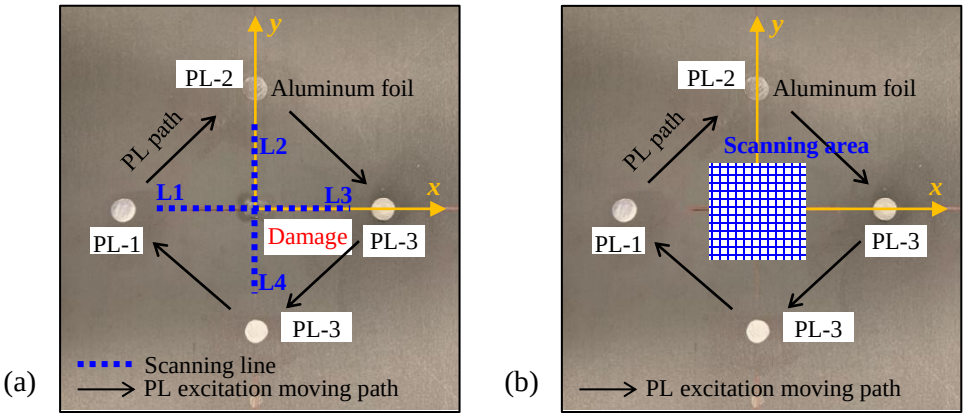

Figure 7.24 Actuation and sensing setup of : (a) 1D inspection, and (b) 2D inspection

7.5.2 1D inspection results

The time-space wavefield acquired by SLDV for the four line-scans with the four different PL excitation locations are plotted in Figure 7.25. The time-space wavefields obtained at PL-1 and PL-3 are along 0 fiber direction, while those at PL-2 and PL-4 are along 90 fiber direction. The time-space wavefields along L2 and L4 obtained with PL-2 and PL-4 are consistent with that obtained using the fixed PL-SLDV NDE system with line scan also along 90 fiber direction as shown in Figure 5.23b. The time-space wavefields obtained at PL-1 and PL-3 are slightly different since the line scans are along 0 fiber direction. Mode conversion S_0 to A_0 and A_0 reflections are observed in all wavefields at 65 mm away from the excitation location where the quartz edge is when the waves interact with the defect. With the automatic PL-SLDV system, valid wavefields are measured and effective inspection purpose is achieved.

7.5.3 2D inspection results

Similar to the data processing of the fixed PL-SLDV NDE inspection results, the time-space wavefields, *f-k* representation at interested frequency 90 kHz, wavefield images, filtering reconstructed images, and space-wavenumber images are obtained at the four excitation locations, and they are plotted in Figure 7.27, Figure 7.28, Figure 7.29, Figure 7.30, and Figure 7.31 respectively. As shown in wavefield snap shots at 53 μs (Figure 7.27), scattered waves are observed when the waves interacted with the damage. The wavenumber spectra at 90 kHz in Figure 7.28 show that scattered A_0 appeared in addition to the incident A_0, and some new wavenumbers (lower than A_0 wavenumber) are observed.

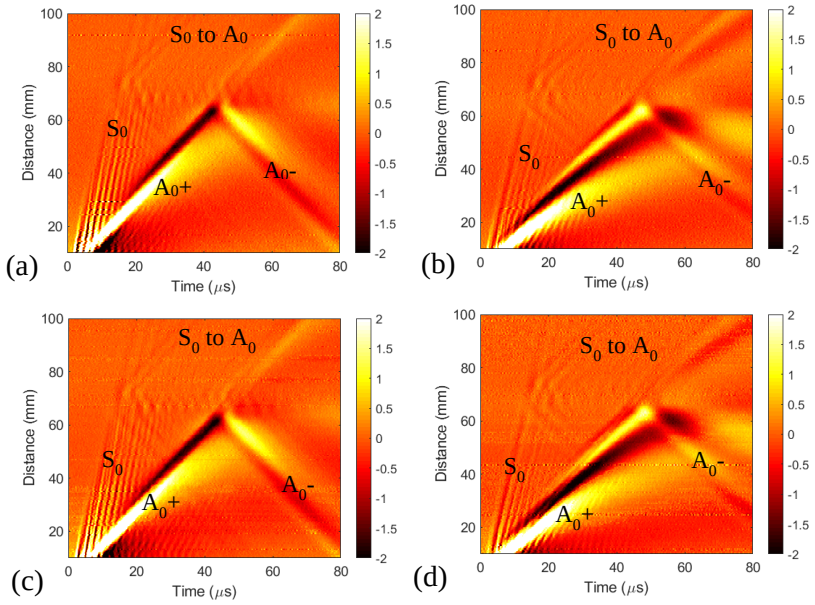

Figure 7.25 Time-space wavefield results of the 1D inspection with automatic PL excitation at: (a) PL-1, (b) PL-2, (c) PL-3, and (d) PL-4, showing that the wavefield results are consistent with those obtained by fixed PL-SLDV NDE system

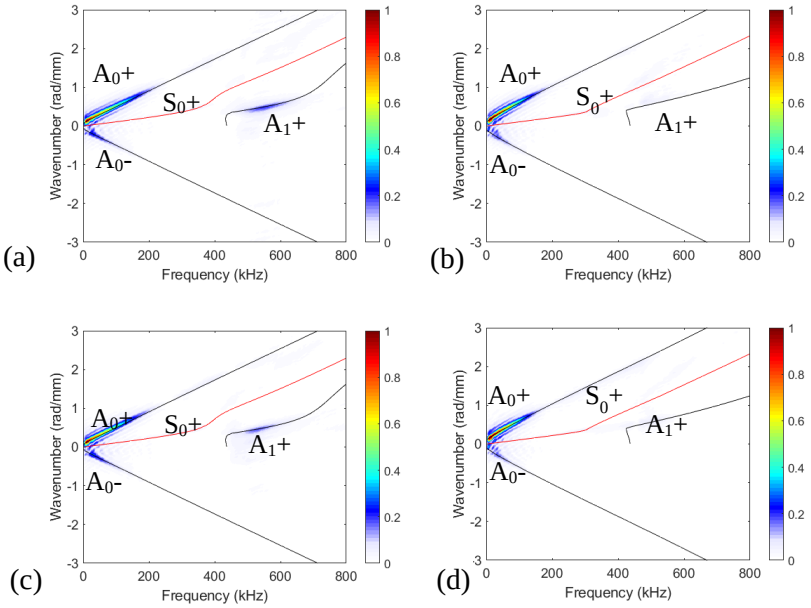

Figure 7.26 *f-k* representation results of the 1D inspection with PL excitation at: (a) PL-1, (b) PL-2, (c) PL-3, and (d) PL-4, showing that the results are consistent with those obtained by laboratory PL-SLDV NDE system

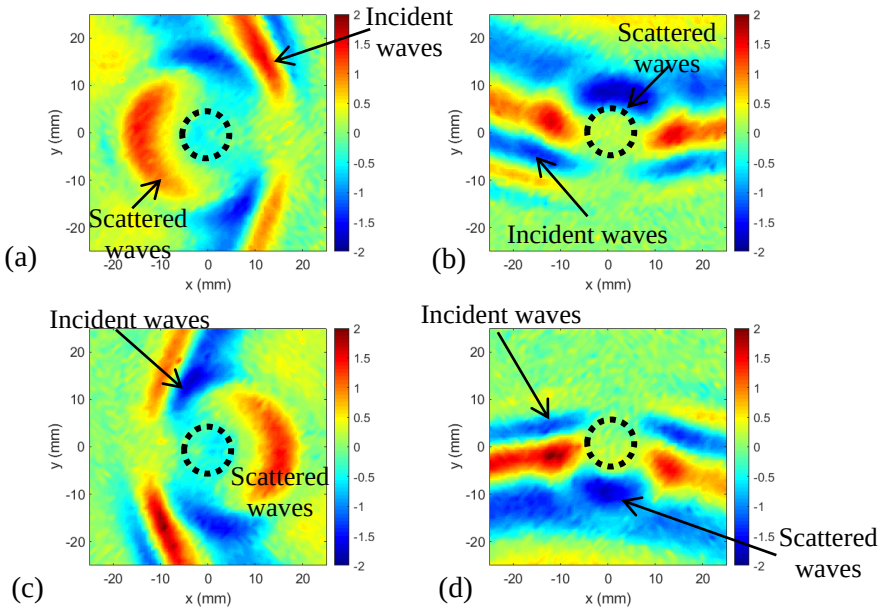

Figure 7.27 Time-space wavefield results of the 2D inspection with PL excitation at: (a) PL-1, (b) PL-2, (c) PL-3, and (d) PL-4, showing that the wavefield results are consistent with those obtained by laboratory PL-SLDV NDE system. Note that the black dash circle showing the quartz location and size

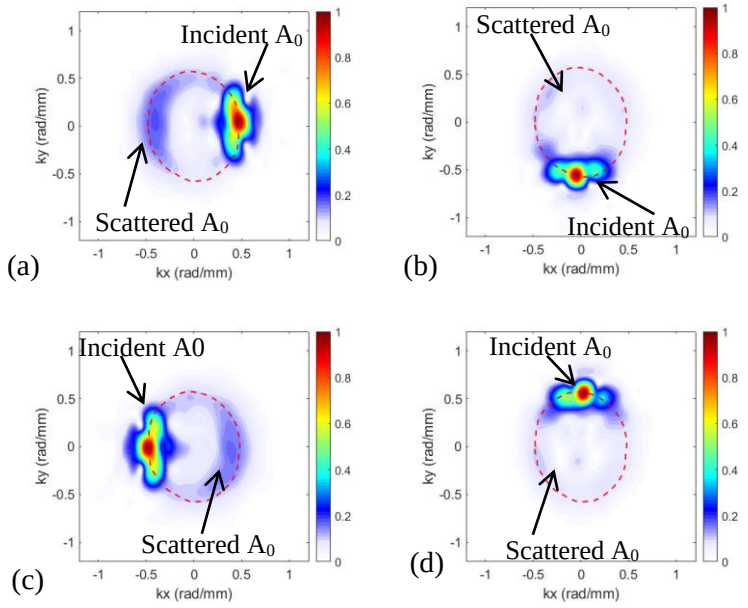

Figure 7.28 *f-k* representation results of the 1D inspection with PL excitation at: (a) PL-1, (b) PL-2, (c) PL-3, and (d) PL-4. Note the red dash line is the theoretical A_0 wavenumber curve at 90 kHz

The wavefield images of the four area scans presented in Figure 7.29 shows obvious energy decrease at the quartz edge w.r.t each inspection location. The filtering reconstructed images at four PL excitation locations (shown in Figure 7.30) clearly show the four edges of the quartz with the high intensity indications. In addition, the space-wavenumber images in Figure 7.31 show the wavenumber change in the damage plate, which highlight the quartz location. The imaging results all showed the presence of the damage with distinguish highlight areas in the intensity maps. The 2D inspection results at four PL excitation locations are consistent with the results in Section 5.4.3 with laboratory setup and are all efficient for damage detection in composite plates.

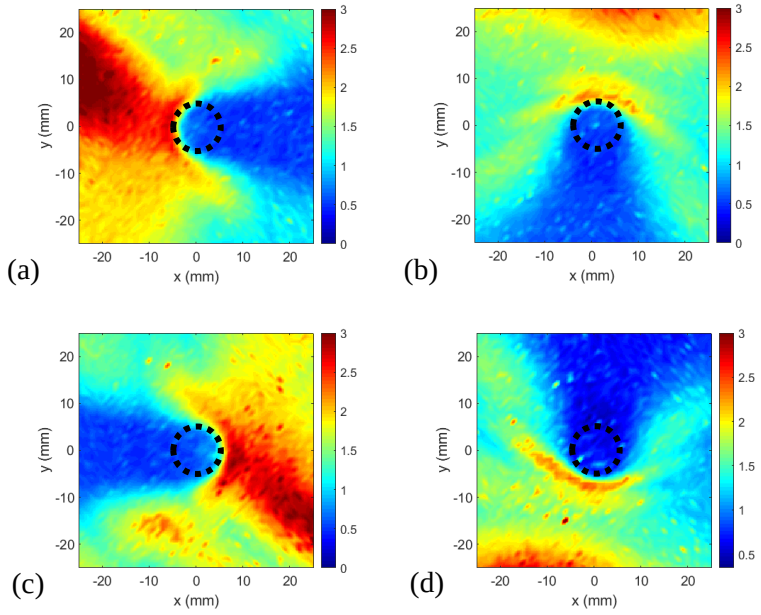

Figure 7.29 Wavefield images with PL excitation at: (a) PL-1, (b) PL-2, (c) PL-3, and (d) PL-4, showing that the four edges the quartz with high intensity areas

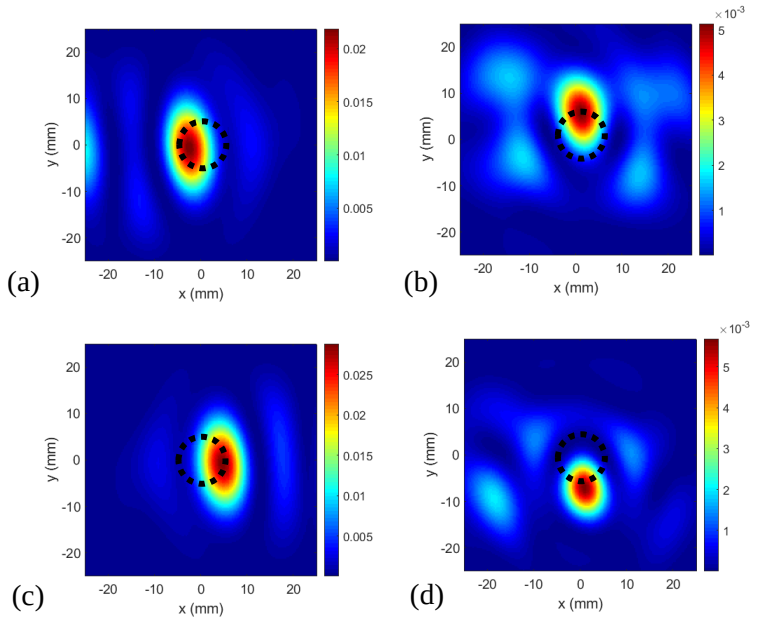

Figure 7.30 Filtering reconstructed images with PL excitation at: (a) PL-1, (b) PL-2, (c) PL-3, and (d) PL-4, showing that the four edges the quartz with high intensity areas

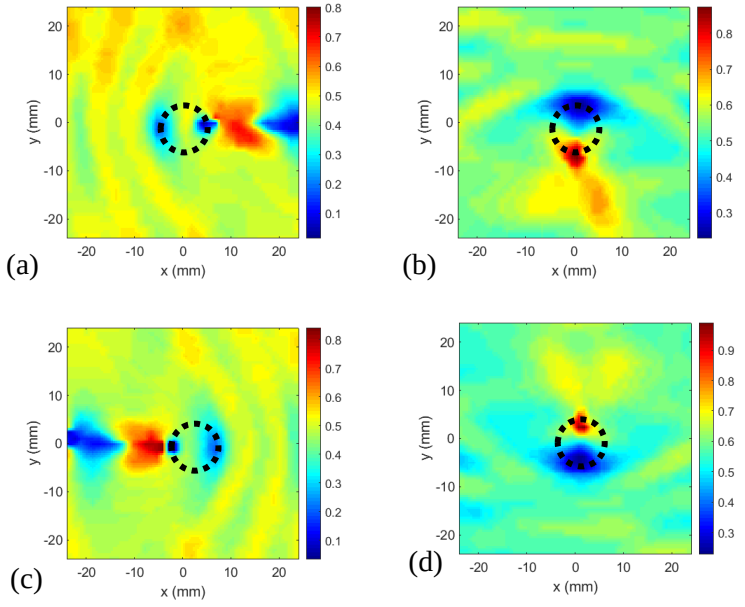

Figure 7.31 Space-wavenumber images of the 2D inspection with PL excitation at: (a) PL-1, (b) PL-2, (c) PL-3, and (d) PL-4, showing the wavenumber change space wisely, which highlight the quartz location

Automatic PL excitation enabled the multi-view inspection of the damage on the target plate; thus, the images can be enhanced through the imaging algorithms based on actuator

network presented in Section 4.4. The resulting imaging results are presented in Figure 7.32. In the synthetic wavefield imaging result (Figure 7.32a), the quartz damage shape and size are both quantified with improved resolution compared to the imaging results obtained by one actuator (Figure 7.29). In the filtering reconstruction imaging result (Figure 7.32b), the damage area is highlighted and the image resolution also improved compared to the results obtained by single actuator, and the damage profile is roughly indicated as a circle shape. Regarding the synthetic wavenumber imaging, the damage is highlighted, and the image resolution improved compared to Figure 7.31, however, the damage profile is not fully quantified. One possible reason is that composite material is anisotropic, wave-interaction along different inspection direction will differ unlike isotropic material.

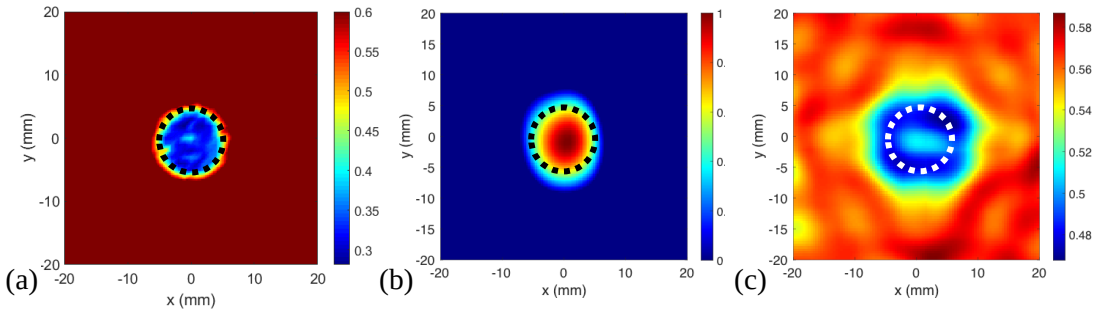

Figure 7.32 Actuator network imaging results: (a) synthetic wavefield image, (b) synthetic filtering reconstruction image, and (c) synthetic wavenumber image

7.5.4 Other PL excitation location schemes

The PL excitation locations can be adjusted by training the KUKA arm at desired points and adjusting the relative scanning grid through SLDV. For demonstration purpose, only 1D inspection is performed for other two PL excitation location schemes: one with 3 excitation locations and another with 8 actuation locations. The two schemes and KUKA moving path are illustrated in Figure 7.33. The 1D time space wavefields obtained with the

two schemes are plotted in Figure 7.34 and Figure 7.35 respectively. One can see that the wavefield results are consistent with previous results and they can be used for further data processing. Moreover, 2D inspection can be performed to obtain the 3D time-space wavefields for further imaging purpose.

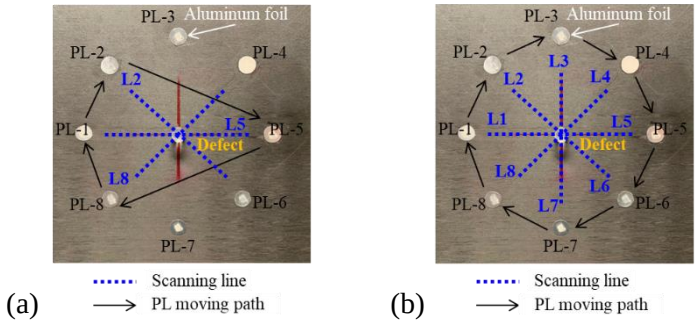

Figure 7.33 Other PL excitation location schemes: (a) one with 3 excitation locations, and (b) another one with 8 actuation locations

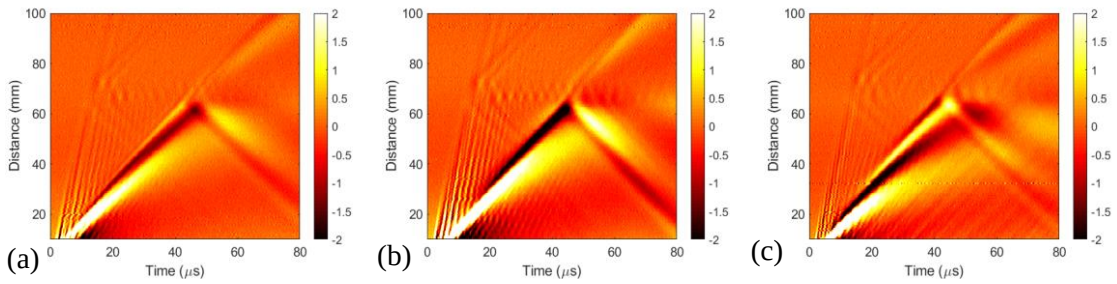

Figure 7.34 1D time-space wavefields with 3 PL excitation locations: (a) PL-2, (b) PL-5, and (c) PL-8

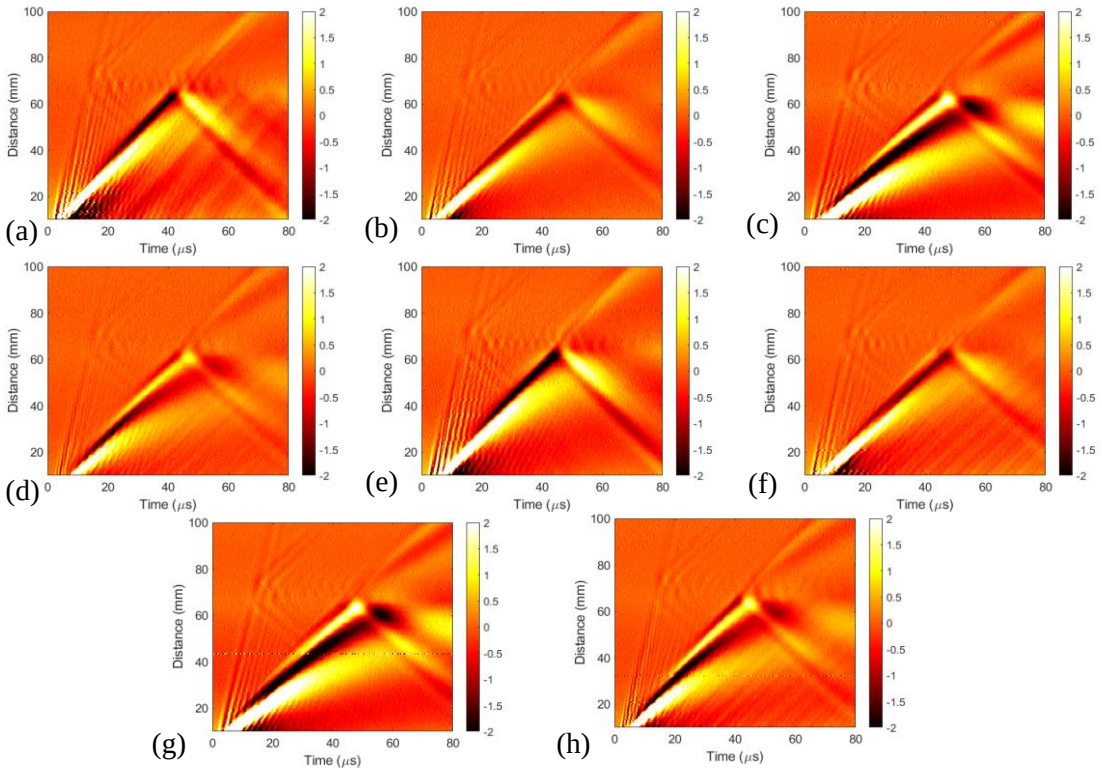

Figure 7.35 1D time-space wavefields with 8 PL excitation locations: (a) PL-1, (b) PL-2, (c) PL-3, (d) PL-4, (e) PL-5, (f) PL-6, (g) PL-7 and (h) PL-8